

AD-A204 981

89 1 18 037

REPORT DOCUMENTATION PAGE

1a. REPORT SECURITY CLASSIFICATION <b>Unclassified</b>		1b. RESTRICTIVE MARKINGS <b>None</b>	
2a. SECURITY CLASSIFICATION AUTHORITY		3. DISTRIBUTION/AVAILABILITY OF REPORT Approved for public release; distribution unlimited. <i>Unlimited</i>	
2b. DECLASSIFICATION/DOWNGRADING SCHEDULE		4. PERFORMING ORGANIZATION REPORT NUMBER(S) <b>Flow Research Report No. 407</b>	
4. PERFORMING ORGANIZATION REPORT NUMBER(S)		5. MONITORING ORGANIZATION REPORT NUMBER(S) <b>AFOSR-TR 87-0786</b>	
6a. NAME OF PERFORMING ORGANIZATION <b>Flow Industries, Inc.</b>	6b. OFFICE SYMBOL (if applicable)	7a. NAME OF MONITORING ORGANIZATION <b>Air Force Office of Scientific Research</b>	
6c. ADDRESS (City, State, and ZIP Code) <b>21414 - 68th Avenue South Kent, WA 98032</b>		7b. ADDRESS (City, State, and ZIP Code) <b>Bldg. 410 Bolling AFB, D.C. 20332-6448</b>	
8a. NAME OF FUNDING/SPONSORING ORGANIZATION <b>AirForce Off. Sci. Research</b>	8b. OFFICE SYMBOL (if applicable) <b>AFOSR/NE</b>	9. PROCUREMENT INSTRUMENT IDENTIFICATION NUMBER <b>F49620-86-C-0092</b>	
8c. ADDRESS (City, State, and ZIP Code) <b>Bldg. 410 Bolling AFB D.C. 20332-6448</b>		10. SOURCE OF FUNDING NUMBERS	
		PROGRAM ELEMENT NO. <b>61102F</b>	PROJECT NO. <b>3005</b>
		TASK NO. <b>A1</b>	WORK UNIT ACCESSION NO.
11. TITLE (Include Security Classification) <b>Cluster Beam Deposition Technology for Optical Coatings</b>			
12. PERSONAL AUTHOR(S) <b>A.C. Day, J.A. Domaradzki, G.S. Knoke</b>			
13a. TYPE OF REPORT <b>Final</b>	13b. TIME COVERED <b>FROM 8/86 TO 2/87</b>	14. DATE OF REPORT (Year, Month, Day) <b>May 1987</b>	15. PAGE COUNT <b>69</b>
16. SUPPLEMENTARY NOTATION			
17. COSATI CODES		18. SUBJECT TERMS (Continue on reverse if necessary and identify by block number)	
FIELD	GROUP	SUB-GROUP	
			<b>Thin films, cluster beam, optical coating (CPS)</b>
19. ABSTRACT (Continue on reverse if necessary and identify by block number)			
<p>An investigation of cluster beam sources for thin-film coating was carried out. Nozzled crucibles of the type used for Ionized Cluster Beam (ICB) deposition were studied to elucidate the make-up of such beams and the mechanisms of cluster formation in them. Work elsewhere has given evidence of 1000-atom clusters and attributed them to homogeneous nucleation in the expanding vapor beam.</p> <p>Homogeneous nucleation theory was used in a computer simulation to calculate cluster nucleation and growth rates. High rates of nucleation were predicted; however, condensation heating of the embryos restricted their final size to a few tens of atoms. It was concluded that large clusters cannot be produced by homogeneous mechanisms alone.</p> <p>A nozzle beam source was constructed and diagnostic methods developed. The experiments confirmed the conclusion of the modeling work and an upper limit was placed on the cluster</p>			
20. DISTRIBUTION/AVAILABILITY OF ABSTRACT <input checked="" type="checkbox"/> UNCLASSIFIED/UNLIMITED <input type="checkbox"/> SAME AS RPT. <input type="checkbox"/> DTIC USERS		21. ABSTRACT SECURITY CLASSIFICATION <b>Unclassified</b>	
22a. NAME OF RESPONSIBLE INDIVIDUAL <b>Capt Kelly</b>		22b. TELEPHONE (Include Area Code) <b>(202) 767-4931</b>	22c. OFFICE SYMBOL <b>NE</b>

populations. However, observations of larger droplets ejected from the source supported a recently proposed heterogeneous theory for cluster beam formation.

Macroclusters of approximately 50 nm diameter were produced in a nozzle beam expanding into a quenching gas. Further work on size control and transport of gas-quenched clusters may result in improved methods for cluster-based coating deposition.

TABLE OF CONTENTS

	<u>Page</u>
LIST OF FIGURES	v
1.0 EXECUTIVE SUMMARY	1
2.0 PHASE I WORK STATEMENT	2
3.0 BACKGROUND OF ICB	3
4.0 MODELING OF CLUSTER FORMATION AND GROWTH	6
4.1 Nucleation and Growth Model	6
4.2 Vapor Flow Model	10
4.3 Results of Calculations	19
4.4 Limitations of Model	25
4.5 Other Mechanisms for Cluster Growth	35
5.0 EXPERIMENTAL DEVELOPMENT	36
5.1 Initial Assumptions	36
5.2 Initial Hardware Design	38
5.3 Beam Ionization and Detection	45
5.3.1 Electron Impact Cross Section for Ionization	45
5.3.2 Detection Efficiency of Apparatus	47
5.4 Performance of Nozzled Crucibles	49
5.4.1 Results of Cluster Detection Experiments	49
5.4.2 Evidence for Heterogeneous Growth of Fine Particles	55
5.4.3 Growth of Ultrafine Particles or Clusters by Gas Quenching	61
6.0 REFERENCES	67
APPENDIX: SUPPLEMENTARY INFORMATION	69

DZIC  
COPY  
INSPECTED

Accession No.	
NTIS	
DZIC	
Index	
Journal	
By	
Date	
Dist	
<b>A-1</b>	

## LIST OF FIGURES

	<u>Page</u>
Figure 1. Typical Apparatus for Ionized Cluster Beam Deposition	4
Figure 2. Film Growth by Cluster Fragmentation	5
Figure 3. Film Growth by Cluster Deformation	5
Figure 4. Area Expansion Ratios for Diverging Nozzles in Water Vapor Experiments	11
Figure 5. Experimental Data of Binnie and Green Compared with Nucleation and Growth Calculations Made by Hill	11
Figure 6. Validation of Cluster Growth Code, Using Conditions for Case 1 of Figure 5	12
Figure 7. Validation of Cluster Growth Code, Using Conditions for Case 4 of Figure 5	13
Figure 8. Areal Expansion of Streamtubes vs. Initial Radial Starting Distance from Nozzle Centerline	16
Figure 9. Distribution of Mass Flux in Free Nozzle Expansion from 20 torr Crucible	17
Figure 10. Beam Expansion Near Centerline as Calculated by Characteristics Method with $P_0 = 20$ torr	18
Figure 11. Calculated Beam Temperature vs. Distance from 0.1 cm Orifice Nozzle	21
Figure 12. Cluster Starting Radius vs. Position at which it Nucleates and Corresponding Final Radius	22
Figure 13. Calculated Beam Temperature vs. Distance from 0.2 cm orifice nozzle	23
Figure 14. Cluster Starting Radius vs. Position at which it Nucleates and Corresponding Final Radius	24
Figure 15. Calculated Beam Temperature vs. Distance from 0.1 cm Orifice Nozzle	26
Figure 16. Cluster Starting Radius vs. Position at which it Nucleates and Corresponding Final Radius	27
Figure 17. Beam Temperature for Run 6 (Evaporation Disallowed)	28

LIST OF FIGURES (CONT.)

	<u>Page</u>
Figure 18. Cluster Initial and Final Radius vs. Nucleation Position for Run 6 (Evaporation Disallowed)	29
Figure 19. Beam Temperature for Run 7 (Evaporation Disallowed)	30
Figure 20. Cluster Initial and Final Radius vs. Nucleation Position for Run 7 (Evaporation Disallowed)	31
Figure 21. Beam Temperature for Run 8 (Evaporation Disallowed)	32
Figure 22. Cluster Initial and Final Radius vs. Nucleation Position for Run 9 (Evaporation Disallowed)	33
Figure 23. Cluster Size vs. Crucible Temperature Differential, from Heterogeneous Theory	36
Figure 24. Electrostatic Energy Analysis of Silver Cluster Beam	38
Figure 25. Schematic Diagram of Apparatus	39
Figure 26. Cluster Beam Source, Ionizer, and Detectors	40
Figure 27. High Vacuum Chamber for Phase I Cluster Beam Study	41
Figure 28. Boron Nitride Crucible in Heater	42
Figure 29. Ionization Stage with Screen Removed	43
Figure 30. Energy Spread of Extracted Ions	44
Figure 31. Focusing Electrostatic Analyzer	45
Figure 32. Electron Impact Ionization Cross Section for Silver	46
Figure 33. Crucible Design for Minimizing Temperature Differential	51
Figure 34. Crucible Temperatures and Deposition Rates During Typical Run	52
Figure 35. Example of Electrostatic Energy Analyzer Results	53
Figure 36. Silver Coating Formed from Nozzle Beam Source	56
Figure 37. Silver Particles and Island Structure from Nozzle Beam Source	57
Figure 38. Aluminum Reacted with Boron Nitride Crucible Lid	58

LIST OF FIGURES (CONT.)

	<u>Page</u>
Figure 39. Silver Droplets on Boron Nitride Crucible after Heating	59
Figure 40. Silver Droplets on Carbon Crucible after Heating	60
Figure 41. Effect of Surface Finish on Droplet Formation in Crucible	61
Figure 42. Particle Growth in Closed Chamber Free with Convective Transport	63
Figure 43. Flow-Controlled Ultrafine Particle Generation and Deposition	64
Figure 44. SEM Photo of 50-100 nm Silver Particles Produced with Nozzled Crucible and Argon Quenching	66

## 1.0 EXECUTIVE SUMMARY

This report covers work performed on Phase I of a Small Business Innovation Research project for AFOSR, on the topic of cluster beam deposition of thin films. The project was intended from the outset to provide a much firmer scientific basis for cluster beam deposition than has existed to date. Weaknesses which were apparent in the literature included: 1) the lack of realistic fluid mechanical treatments in models of the cluster growth environment; and 2) inadequate methods of beam characterization. It was felt that Phase I work could result in significant contributions by addressing these problem areas, due to the current interest in clusters and the unique film structures which may be possible using cluster beams.

Modeling work performed on the project used the method of characteristics to generate beam expansion rates, including some off-axis cases. These rates were then used in homogeneous nucleation and growth calculations. It was found that nucleation rates were high, but that clusters could grow very little, due in part to the increase in temperature experienced through condensation heating. Beam expansions calculated from the characteristics method generally led to somewhat less cluster growth than when simple  $30^\circ$  expansions were assumed, as has been common in the literature.

With condensation heating neglected, clusters of up to approximately 42 atoms could be predicted. Preliminary calculations of radiant cooling by the clusters were performed which showed that a potentially important mechanism has not been accounted for previously. A full treatment of this mechanism could not be carried out within the constraints of the project but may be treated in a subsequent publication.

A general conclusion of the modeling task was that homogeneous nucleation can probably condense no more than about 1% of the metal vapor flux into clusters. This conclusion is based on calculations for the simple nozzle beam sources described in the literature, and for the time being neglects the possibility of radiant cooling.

The experimental work included the construction and testing of a complete cluster beam apparatus, including nozzled crucibles and heaters, ionizing stage, electrostatic energy analyzer, and ion collector. The detection efficiency of the apparatus was determined for metal and residual gas detection efficiency. By such methods it was determined that a beam mass fraction of  $3.7 \times 10^{-4}$  could be detected for all clusters in the size range of 400-600 atoms per cluster, and  $5.6 \times 10^{-4}$  for all clusters in the 800-1200 range. For monoenergetic/monodisperse clusters, the limits are lower by about a factor of ten.

A large number of experiments were run with silver and aluminum throughout the vapor pressure regime of 1 to 16 torr. No peaks definitely attributable to clusters were seen in the analyzer data, which would have shown clusters of up to 2000 atoms per cluster. Thus, conditions for cluster production and measurement were carefully controlled; if upwards to 30% of the beam can be made into clusters as has been claimed elsewhere, they should have been detectable.

In spite of this result, it was found that the nozzled source did produce a considerable amount of small particles which could be seen directly or with a microscope. The conditions under which these particles were produced were studied. These studies support a new theory of heterogeneous cluster formation on inner crucible surfaces developed by Knauer. The heterogeneous theory places more stringent requirements on crucible temperature control than the homogeneous mechanism; it is possible that particles or clusters in the desired size range could be made in a source with two or more independent temperature zones.

Workers at Hughes have recently seen evidence of 600 atom (3 nm) clusters but at the 1% level or less. One option for future cluster deposition work is to attempt a more rigorous crucible re-design, in order to optimize for the heterogeneous cluster growth mechanism. Two factors persuaded us not to take this approach further than the effort already described in Section 5.4.2: 1) the heterogeneous theory cannot yet provide rigorous design information, and 2) intuitively, it appears unlikely that clusters formed on surfaces and then entrained in the nozzle flow could comprise a significant fraction of the beam mass.

An alternate approach, based on growth and transport of ultrafine particles or clusters in a quenching gas, appears more promising in our view and has been proposed for Phase II development. This report described a test which showed that such particles could be produced in our apparatus. The problems of gas/particle transport and separation appear to be solvable and are addressed in the Phase II proposal. Most of the theoretical and experimental capabilities developed in Phase I work can be applied directly, since nozzle gas flows and beam characterization will continue to be of central importance. The great range of particle sizes obtainable with gas-quench techniques, and the high mass utilization factor, should significantly extend the possibilities for cluster deposition in the future.

## 2.0 PHASE I WORK STATEMENT

The Phase I Work Statement of research tasks is shown below for reference, as given in the contract instrument:

- (1) Numerically model cluster formation using nucleation theory or the appropriate kinetic theory.
- (2) Seek experimental confirmation of cluster formation in collaboration.
- (3) Ascertain the charged species present in the ionized cluster beam.
- (4) Attempt to deposit and characterize films using this technique.

### 3.0 BACKGROUND OF IONIZED CLUSTER BEAM DEPOSITION

The field of cluster science is by now a broad one and no attempt will be made to review it here. However, it is useful to examine the context in which cluster beam deposition developed and to comment on the current status of the technology.

Cluster science began as a fascination with things that happen in supersonic nozzle sources, first described by Kantrowitz and Gray (1951). They predicted that a gas passing through a small orifice into vacuum would cool substantially, transferring most of its random thermal energy into forward-directed kinetic energy. This led to atomic and molecular beam sources of high intensity. It was later found that under certain conditions a highly supersaturated state existed in the beams, leading to nucleation and growth of gas clusters. Typical sizes ranged from  $10^2$  to  $10^5$  molecules per cluster. Characterization of these cluster beams became an active area of research through the sixties and early seventies. Probably the best review of the work through this period is an article by O.F. Hagen (1974).

The early and mid-seventies also saw the beginnings of a strong interest in new thin film technologies, particularly those involving ion-activated deposition. Taken as a class, these methods offered better film strength, adhesion, and density. Certain drawbacks were also noted such as radiation damage to electronic circuits during metallization processes, implantation of ionized impurities into films, and difficulties in controlling beams with low mass-to-charge ratios.

Work on Ionized Cluster Beam deposition was begun in this period by Takagi and co-workers at Kyoto University (Takagi, 1975). A nozzle source similar to those used for gas clusters was found to produce large metal clusters as well. By charging massive clusters instead of individual atoms, it was reasoned, one could obtain activated deposition without entailing any of the drawbacks noted above. A typical source apparatus including cluster ionization and acceleration components is shown in Figure 1. A number of application-oriented papers by Takagi's group showed considerable promise for the technique, even though the distinguishing mechanism for film growth had not been conclusively demonstrated. The mechanism proposed by Takagi was that of total breakup of the clusters on impact and partitioning of the cluster energy into surface migration energy of atoms, as shown in Figure 2.

Another mode of growth involving compaction and flattening has recently been predicted through molecular dynamics calculations (Mulle, 1987). Examples of his results are shown in Figure 3. The molecular dynamics approach measures surface mobility of individual atoms, but it is interesting to observe that something like a plasma sprayed coating might be possible on a nanometer scale. This could lead to better films by reducing the tendency to form loose columns during growth.

The results reported by Takagi began to arouse interest outside Japan in the early eighties. ICB systems were being used on a commercial scale in Japan and a licensing agreement with the Eaton Corporation made a system available in the U.S. Unfortunately, the Eaton systems lacked the sort of beam characterization facilities which most researchers required. It became clear that laboratories interested in the potential benefits of cluster deposition would have to develop their own techniques and equipment.

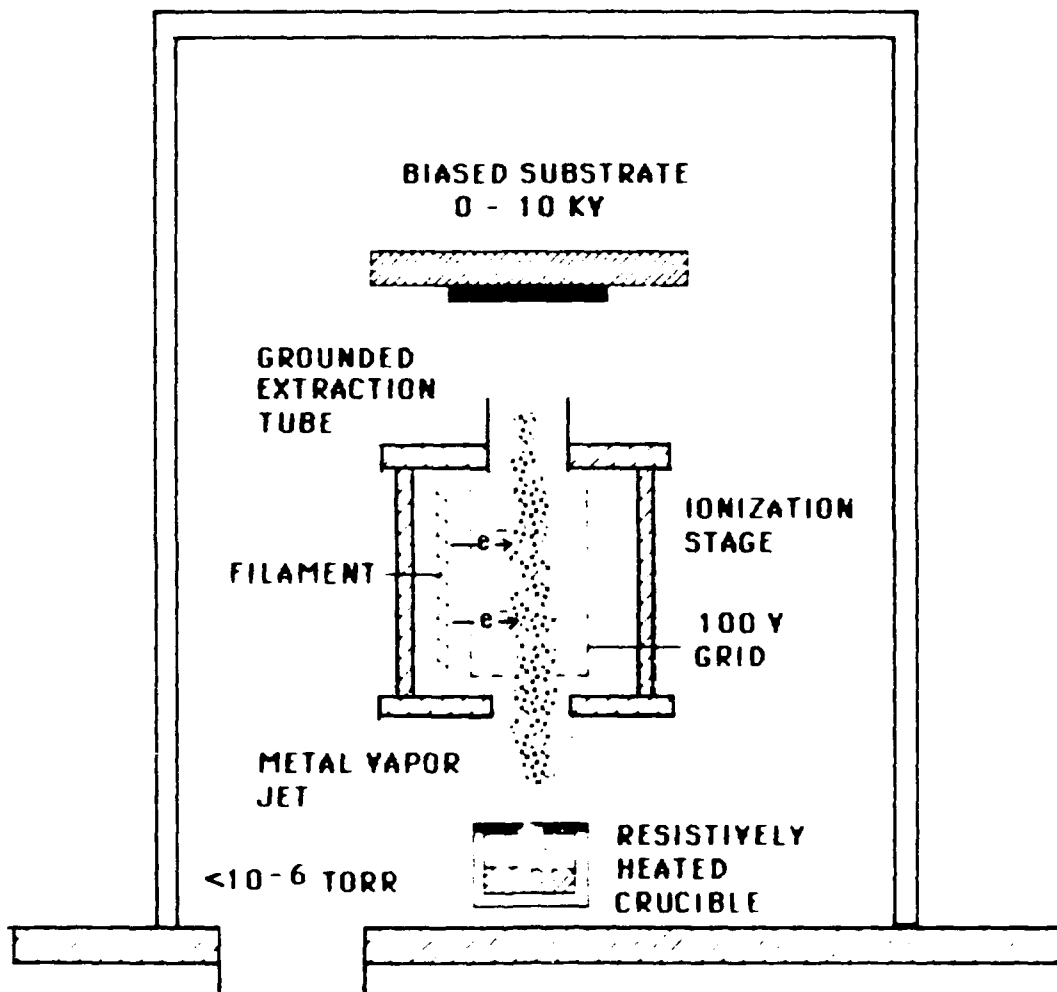


Figure 1. Typical apparatus for ionized cluster beam deposition.

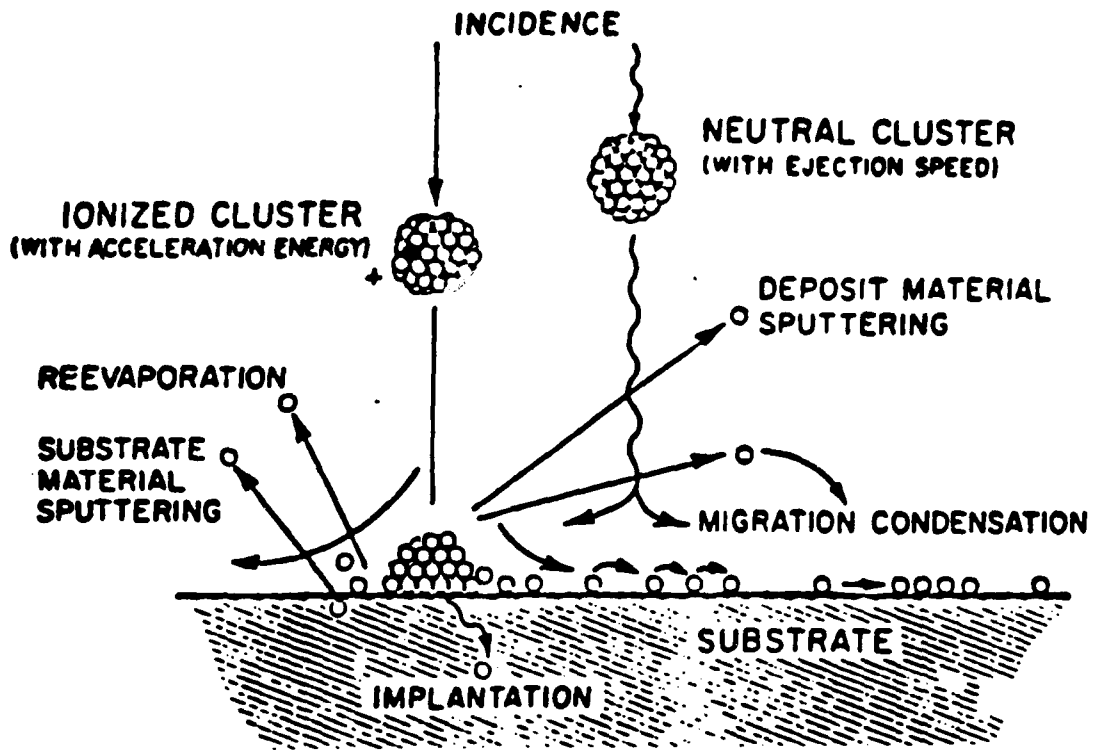


Figure 2. Film growth by cluster fragmentation.

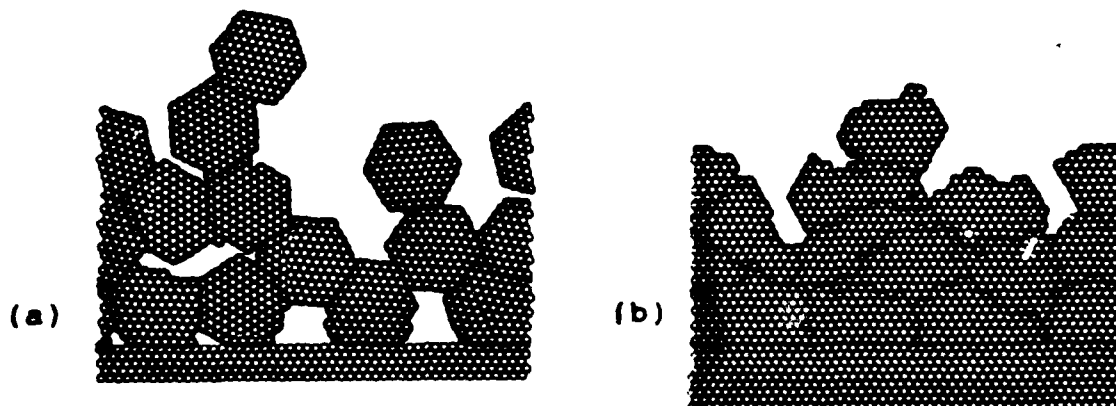


Figure 3. Film growth by cluster deformation (a) with  $E=0.2$  eV/atom, (b) with  $E=3$  eV/atom (From Muller, 1987).

Since then there has also been some controversy regarding the possibility of condensing metals in a pure vapor expansion. The primary difficulty is that a great deal of latent heat must be released in forming clusters. In most cluster sources this heat is gradually taken up by a large number of inelastic collisions. A pure vapor can take up some of its own latent heat in this way, but it is far easier to "seed" metal clusters in a flow of inert quenching gas. Sources which use an oven or pulsed laser to vaporize a metal into a gas are now a mainstay of research in the chemistry and physics of small clusters.

Takagi has steered away from the gas-quenching approach, possibly to avoid the apparent complication due to gas flows. A number of phenomena such as convection and nozzle clogging by cluster impaction must be considered. However, these are essentially transport problems. The reliability and efficiency with which gas-quenched sources produce clusters leads us to believe that ways should be found to exploit these as well. This has been tried with some success by Kuiper (1981). We have proposed for Phase II work a variant on this technique, employing a more sophisticated approach to the problems of gas flow and control. Because larger clusters or particles (greater than 5 nm) can also be made by such methods, the deformation mode of film growth should apply (Figure 2), thus offering more radical departures from current deposition technologies.

#### 4.0 MODELING OF NOZZLE BEAM EXPANSION AND CLUSTER GROWTH

##### 4.1. Nucleation and Growth Model

We have performed numerical modeling of the physical phenomena involved in the process of nucleation when a gas expands into vacuum through a supersonic nozzle. For a gas to condense, it has to be brought to a supersaturation state where the pressure and temperature of the gas fall into the region of the P-T plane where only liquid phase may exist under equilibrium conditions. This generally leads to some combination of gas cooling and a rise in pressure to bring the system toward an equilibrium state. In the case of a one dimensional gas flow through a supersonic nozzle, the thermodynamic state of the gas is determined entirely by the cross-sectional area of the beam if the expansion may be considered isotropic. The cross-sectional area  $A(x)$  is related to the Mach number  $M(x)$  by the equation

$$A(x)/A(0) = \frac{1}{M(x)} \left[ \frac{2}{\gamma+1} \left( 1 + \frac{\gamma-1}{2} M(x)^2 \right) \right]^{\frac{\gamma+1}{2(\gamma-1)}} \quad (1)$$

where  $x$  is the axial distance from the nozzle,  $A(0)$  is the cross-sectional area of the nozzle throat, and  $\gamma$  is the specific heat ratio. From equation (1), the Mach number at the throat is  $M(0)=1$ .  $M(x)$  can be computed if the area ratio  $A(x)/A(0)$  is known as a function of the distance  $x$  from the throat. The pressure and the temperature of the gas are then determined with the following gasdynamics formulas:

$$P = P_0 \left[ 1 + (\gamma-1)M^2/2 \right]^{-\gamma/(\gamma-1)} \quad (2)$$

$$T = T_0 \left[ 1 + (\gamma-1)M^2/2 \right]^{-1} \quad (3)$$

where  $P_0$  and  $T_0$  are stagnation pressure and temperature, i.e., pressure and temperature at the source where the gas velocity is zero. For the flow beyond the sonic point ( $x=0$ ) the Mach number is typically greater than unity and increases rapidly with the distance from the throat, equation (3). The gas is then cooled rapidly and may reach a supersaturated state. Such qualitative reasoning forms the basis of the explanation of the experimentally observed phenomenon of cluster formation in nozzle beam sources.

To describe the process of cluster formation in a more quantitative way, we have adopted the following approach. The expansion of the gas is assumed to be a one-dimensional steady state flow so that all physical quantities depend only on the variable  $x$  which measures distance from the nozzle throat. The governing equations for the one-dimensional flow include the continuity, momentum, and energy equations and contain the effects of nucleation as obtained from the classical nucleation theory, as well as cluster growth due to condensation. These equations are (Hill, 1966):

$$\frac{dP}{dx} = P \left[ (\lambda-1) \frac{d\mu}{dx} - \frac{1}{A} \frac{dA}{dx} \right] / \left[ 1 - (1-\mu) \frac{\gamma-1}{\gamma} + \frac{1}{\gamma M^2} \right] \quad (4)$$

$$\frac{dT}{dx} = T \left[ \lambda \frac{d\mu}{dx} + \frac{\gamma-1}{\gamma} (1-\mu) \frac{1}{P} \frac{dP}{dx} \right] \quad (5)$$

$$\frac{dM}{dx} = M \left[ -(1-\mu) \frac{1}{P} \frac{dP}{dx} / (\gamma M^2) - \frac{1}{2T} \frac{dT}{dx} \right] \quad (6)$$

$$\frac{d\mu}{dx} = \frac{\rho_L}{\dot{m}} \left[ Q_1 \frac{1}{u} \frac{dr}{dt} + \frac{4\pi}{3} I A r_o^3 \right] \quad (7)$$

$$\frac{dQ_1}{dx} = Q_2 \frac{1}{u} \frac{dr}{dt} + 4\pi I A r_o^2 \quad (8)$$

$$\frac{dQ_2}{dx} = Q_3 \frac{1}{u} \frac{dr}{dt} + 8\pi I A r_o \quad (9)$$

$$\frac{dQ_3}{dx} = 8\pi I A \quad (10)$$

In the above equations, P is pressure, T the temperature, M the Mach number,  $\mu$  is the ratio by mass of liquid and vapor phases, A the beam cross-sectional area,  $\lambda = h/c_p T$  where h is the enthalpy of the gas-liquid transition and  $c_p$  is the specific heat at constant pressure,  $\gamma$  is the ratio of specific heats at constant pressure and volume,  $\rho_L$  is the density of the liquid,  $\dot{m}$  is the total flow rate, I is the nucleation rate,  $r_0$  is the radius of the nucleating drops, u is the velocity of the gas, and  $dr/dt$  is the drop radius growth rate.  $Q_1$ ,  $Q_2$ , and  $Q_3$  are auxiliary variables related to the total number of condensed droplets and their total surface area so that the surface averaged drop radius is

$$\bar{r} = \sqrt{2Q_1/Q_3} \quad (11)$$

We assumed that at location x, droplets with the radius  $r_0(x)$  are spontaneously created at the rate (per unit volume)  $I(x)$  given by the classical nucleation theory (Frenkel, 1946):

$$I = \left(\frac{P}{kT}\right)^2 v \sqrt{2\sigma/m} \exp\left(-4\pi\sigma^2 r_c^3 / 3kT\right) \quad (12)$$

where  $\sigma$  is the surface tension of the liquid, m is the mass of one molecule, v is the volume of one molecule in the liquid, k is the Boltzmann constant, and  $r_c$  is the critical radius at temperature T and pressure P. The critical radius is given by

$$r_c = \frac{2\sigma m}{\rho_L kT \ln(P/P_g)} \quad (13)$$

where  $P_g(T)$  is the flat-film saturation pressure. The drop growth rate is then determined from the equations relating the net mass flow to and from the droplet surface due to condensation and re-evaporation.

$$\frac{dr}{dt} = \frac{\zeta}{\rho_L} (\beta - \beta_D) \quad (14)$$

where  $\zeta$  is the condensation coefficient (usually assumed to be close to unity), and  $\beta$  and  $\beta_D$  are the condensation and evaporation rates, respectively. The condensation rate is the mass flux to the surface of the drop (per unit area, per unit time) and is given by the expression derived from the kinetic theory

$$\beta = P / \sqrt{(2\pi k T/m)} \quad (15)$$

Similarly, the evaporation rate is given by

$$\beta_D = P_D / \sqrt{(2\pi k T_D/m)} \quad (16)$$

where  $P_D$  and  $T_D$  refer to the pressure of the liquid drop and to its temperature, respectively. The pressure  $P_D$  is the pressure of the equilibrium vapor-liquid state at temperature  $T_D$  corrected for the effects of the surface tension for the drop with radius  $r$ :

$$P_D = P_s(T) \exp(2\sigma_m/(\rho_L k T_D r)). \quad (17)$$

The temperature of the drop is usually higher than the temperature of the condensing vapor because of the latent heat release. This can amount to differences of tens or hundreds of degrees, depending on the latent heat of condensation, and thus strongly affects the re-evaporation rate. This effect has not been accounted for in some of the recent literature on cluster beam modeling. This points out the virtual necessity of removing the latent heat by collisions with an inert background gas, as we plan to do in the Phase II work. The drop temperature is computed from the following algebraic equation:

$$K\zeta(1-\beta_D T_D/\beta T) - K(1-\zeta) \alpha \left( \frac{T_D}{T} - 1 \right) + \zeta(1-\beta_D/\beta) (\lambda-1) \frac{\gamma}{\gamma-1} = 0 \quad (18)$$

where  $K = (\gamma+1)/2(\gamma-1)$  is the average specific energy of the arriving molecules and  $\alpha$  is the thermal accommodation coefficient which is always close to the unity.

Finally, it is assumed that the vapor satisfies the perfect gas law

$$P = \rho kT/m \quad (19)$$

which also gives a simple expression for the speed of sound

$$c = \sqrt{\gamma kT/m} \quad (20)$$

and the Mach number  $M = u/c$ .

### The Numerical Method

Equations (4)-(10) with (16) and (18) describe one dimensional gas flow with condensation. To solve these equations, numerical methods must be used. Equation (18) was solved by the bisection and secant method (Dahlquist & Bjork, 1974) and equations (4)-(10) by the fourth order Runge-Kutta method, as suggested by Hill (1966).

The numerical method was tested by repeating some of the calculations reported by Hill (1966) for water vapor condensing in a supersonic nozzle of prescribed geometry. Agreement was good, predicting droplet formation of 3.7% of the vapor with average droplet size of 17 nm. These numbers correlated well with experiments referenced by Hill. Area distributions for different

nozzles considered by Hill are reproduced here as Figure 4. Figure 5 shows results of his calculations for different values of the stagnation pressure and temperature for one of those nozzles. In Figures 6 and 7, we show results of our calculations for two cases denoted as 1 and 4 in Figure 5. Both figures clearly show departures of the computed pressures from the isentropic (lower) curves, indicating the onset of condensation. Our calculations are also in good agreement with the results of Hill (Figure 5). The only difference is that in our calculations, the condensation seems to start slightly earlier. The probable reason for this discrepancy is our approximation of the area distribution of the experimental nozzle from Figure 4 by a parabolic expansion fitted at  $x=0.5$  and  $10\text{cm}$ , which leads to a slightly higher expansion ratio than the original nozzle. Considering other sources of discrepancy such as the possible use of different expressions for the saturation pressure (not given by Hill) in the literature, and scatter in the experimental data, the agreement between the two sets of calculations is sufficient to validate our numerical code.

#### 4.2 Vapor Flow Model

The next step was to properly calculate the rate of expansion of a free vapor jet, an approach not yet taken elsewhere. The expansion of a molecular beam into vacuum is very different from the flow through a long diverging nozzle since there are no walls to keep the flow within prescribed boundaries. This difficulty is usually circumvented by assuming that the expanding flow has a conical shape within a prescribed apex angle of about  $20\text{--}30^\circ$  (Usui et al., 1985, Yang & Lu, 1986). In this research, we used two different ways of determining the area distribution of the expanding supersonic flows. One is consistent with the above described assumption of the conical flow and the other determines the area distribution from equation (1) with the Mach number obtained from the solution of the full gasdynamics equations for the axisymmetric, isentropic flow expanding from the cylindrical nozzle into vacuum. The latter approach, which should be more realistic, will be briefly described below.

The flow of the metallic vapors through the orifice was modeled as a two-dimensional axisymmetric nozzle flow using the method of characteristics. This method provides detailed flow information, including the angular distribution of mass flux. The calculation begins at the most constricted part of the flow (the nozzle exit) which is the sonic point ( $M=1$ ). Because the gas flow beyond this point is decoupled from disturbances upstream, it is only necessary to find  $P$  and  $T$  at  $M=1$  to carry out the computations in the expansion region. These quantities are obtained from equations (2) and (3) above. While it is possible that some nucleation and growth occurs before the sonic point, calculations by Yang and Lu (1986) indicated that subsonic clustering was almost negligible.

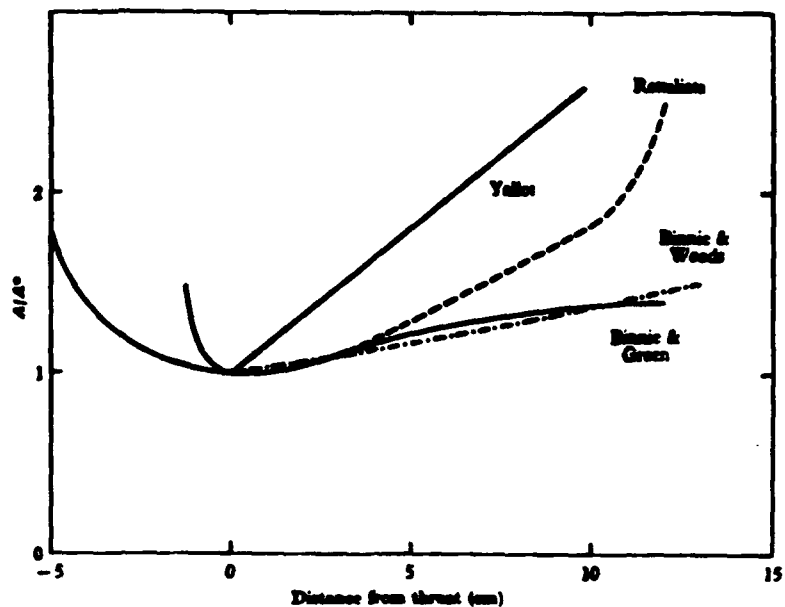


Figure 4. Area expansion ratios for diverging nozzles in water vapor experiments (from Hill, 1966).

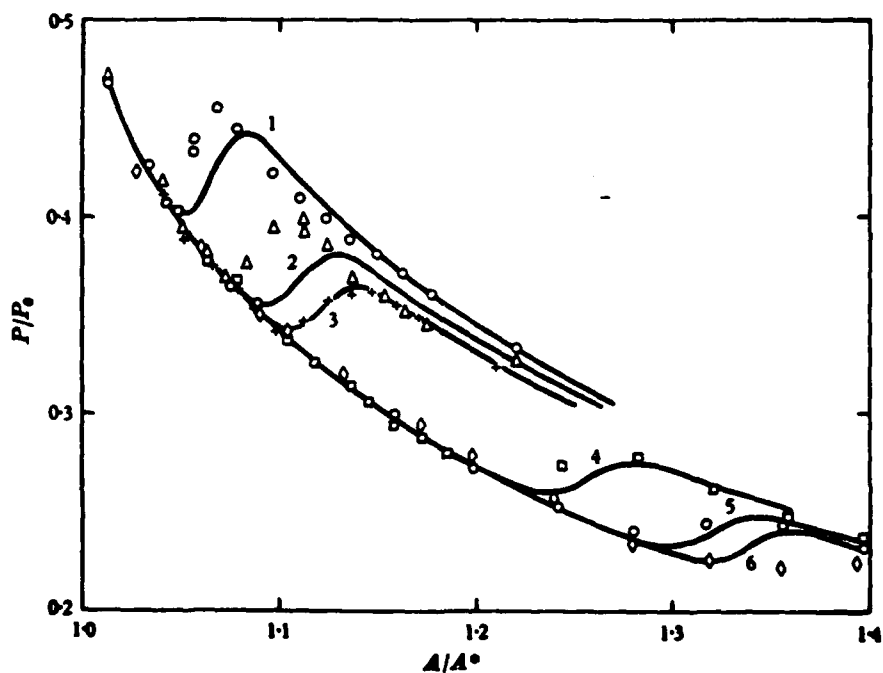


Figure 5. Experimental data of Binnie and Green compared with nucleation and growth calculations made by Hill (1966).

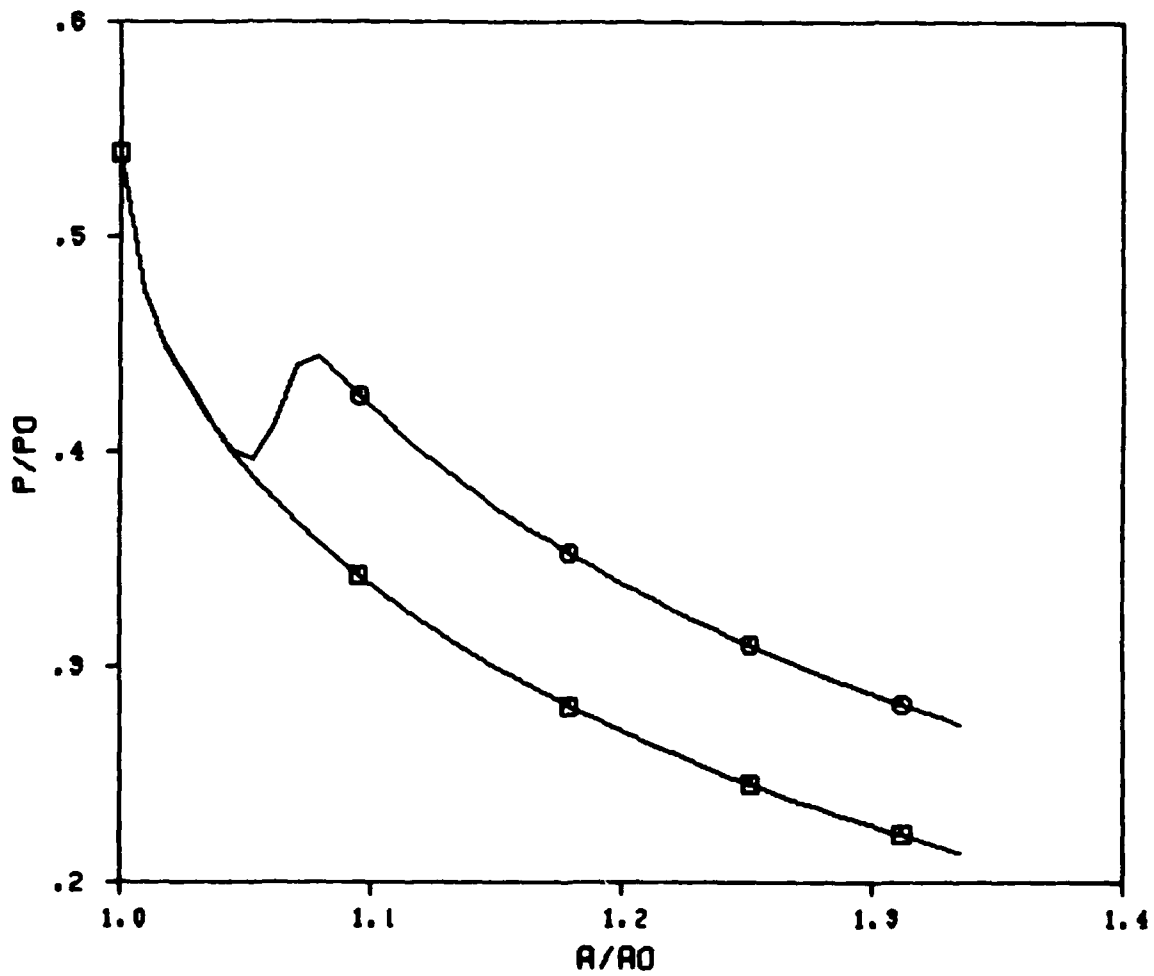


Figure 6. Validation of cluster growth code, using conditions for Case 1 of Figure 5 (Binnie and Green nozzle,  $P_0 = 0.647$  atm,  $T_0 = 101^\circ\text{C}$ ).

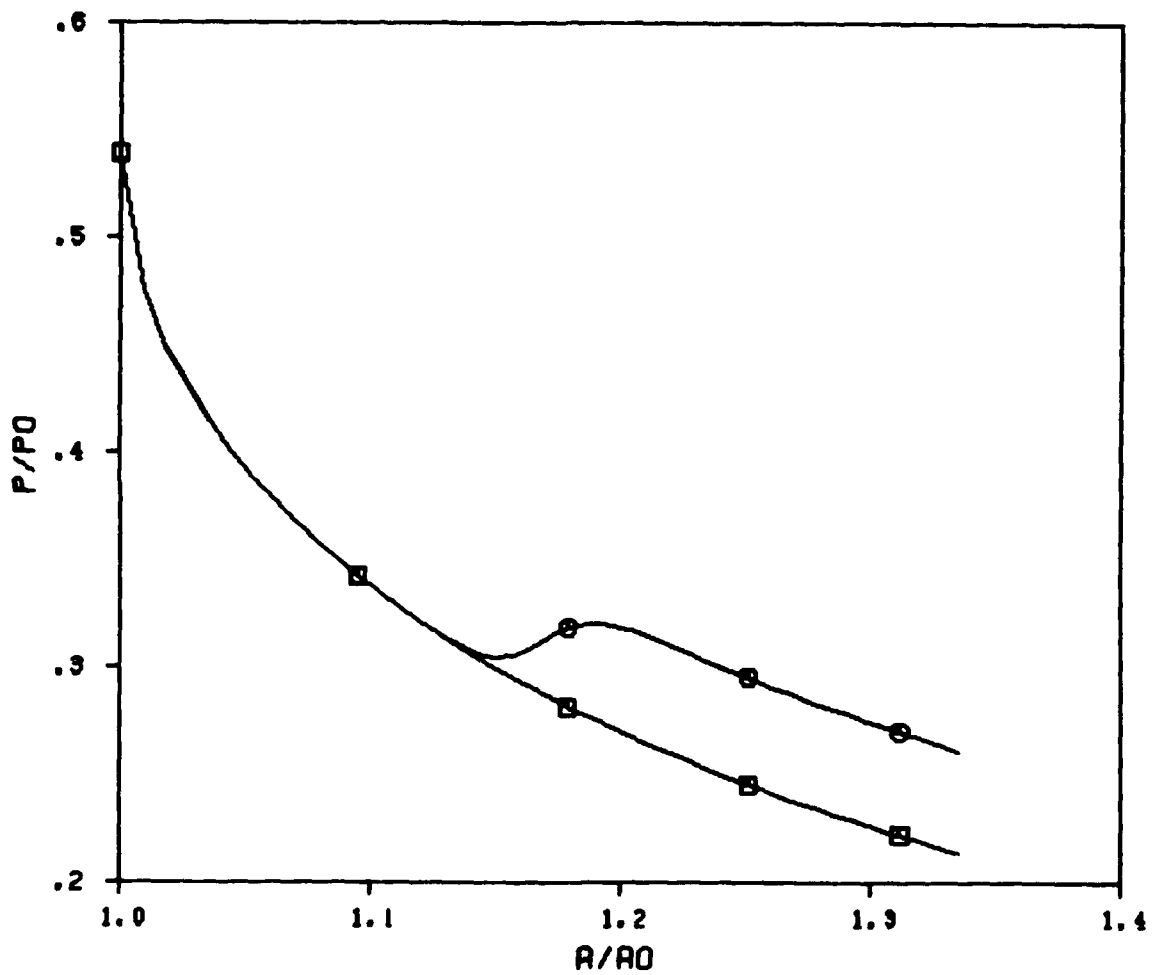


Figure 7. Validation of cluster growth code, using conditions for Case 4 of Figure 5 (Binnie and Green nozzle,  $P_0 = 0.646 \text{ atm}$ ,  $T_0 = 127^\circ\text{C}$ ).

The method of characteristics described by Shapiro (1954) is used for exact stepwise numerical calculation of axisymmetric supersonic flows. The flow is also assumed to be steady and irrotational. The method of characteristics solves for the flow field parameters by following right-running and left-running Mach lines (characteristics) which trace axisymmetric compression and expansion waves. Because the waves weaken as they move away from the axis of symmetry and strengthen as they move towards it, the equations of motion must be integrated for the strength of the waves as well as their location. Thus there are four unknowns to solve for at each intersection of right-running and left-running characteristics: the axial location  $x$ , the radial location  $r$ , the velocity  $V$  and the flow directional angle  $\theta$ . The four equations for the unknowns are written in terms of known information at another point on the right-running characteristic and another point on the left-running characteristic. When parameters vary along the characteristic between the known point and the unknown point, the average value is used.

Depending upon what additional information is known at the unknown point, the solution of the four equations takes various forms:

- (1) The basic case is the free intersection of two characteristics.
- (2) If the unknown point is on the axis of symmetry, then  $r$  and  $\theta$  are known to be zero, so the problem is reduced to two unknowns.
- (3) If one of the known points is on the axis of symmetry, then a special form of the equations for the four unknowns must be used because the equations are indeterminate on the axis. The limit of the indeterminate value as the characteristic approaches the axis is used.
- (4) If the unknown point is on the wall, then the flow angle is known from the wall angle. Three equations are solved for  $x$ ,  $r$ , and  $V$ .
- (5) If the characteristic runs uninterrupted from the axis of symmetry to the wall, then yet another form of the equations is used, incorporating the limits on the axis and the wall angle.
- (6) If the unknown point is on the edge of the flow field, where in actuality a mixing layer exists, then the flow velocity can be found from matching the jet's pressure with the ambient pressure. This leaves three equations for  $x$ ,  $r$ , and  $\theta$ .

The characteristics method is useful only in regions where the mean free path between collisions is small. The mean free path is inversely proportional to the number density of the molecules and the effective collision cross section. In the vapor above liquid aluminum at 2139 K and 20 torr, the mean free path is about 0.0012 cm. When the vapor is expanded through a nozzle, however, the mean free path increases to about 0.25 cm at the point where  $M=10$ . When the mean free path approaches the physical dimensions of the device, further fluid flow calculations become meaningless, since the trajectories of the molecules will be unchanged by intermolecular collisions (a condition known as free molecular flow). Since the method of characteristics experienced convergence stability problems at high Mach numbers, the calculation was terminated when the Mach number exceeded the limit for free molecular flow. This generally did not occur until the flow was many nozzle diameters beyond the orifice.

Primarily, the method of characteristics code was used to generate the flow expansion ratio  $A(x)/A(0)$  along streamtubes for use in the condensation computer model (as input to equation (1)). The flow area  $A(x)$  of the streamtube is referenced to the flow area of the streamtube at the sonic point  $A(0)$ , where the flow velocity is equal to the speed of sound. Figure 8 shows several streamtube area histories from the 2-D method of characteristics calculation compared with the usual choice of one-dimensional flow in a 30 degree cone. The 2-D area histories are seen to depend strongly on the starting position (radial distance from centerline) of the streamtube in the orifice. This information was used in the cluster growth code to determine whether significant differences in the sizes or numbers of clusters should occur off axis.

The final flow angle of the streamtubes is another useful output of the characteristics model. This information can be used to estimate the mass deposition rate as a function of position on a substrate. The thickness profile of a deposited film can then be used to test the model; experimental data showed good agreement with predictions, as will be shown in a later section.

The mass flux of the whole orifice flow field is shown in Figure 9. The length of the vectors is proportional to the mass flux  $= \rho v$ , where  $\rho$  is the density and  $v$  is velocity. The direction of the vectors is the flow angle. It can be seen that the orifice flow at 20 torr is peaked toward the center but is not strongly directional.

Expansion ratios were calculated for  $P_0 = 1, 2, 5, 10$  and 20 torr, but were found to be virtually identical for axial streamtubes. In reality, some differences should appear when  $P_0$  is a few torr or less because of boundary layer effects in the nozzle. The nucleation and growth work gave significant condensation only at the higher pressure, however, where such effects should be negligible.

In Figure 10, we present results for the area expansion ratio for aluminum vapor expanding into vacuum through a cylindrical nozzle 1 mm in diameter. In this figure, results computed from the axisymmetric method of characteristics are compared with the area distribution for the conical flow of 30° apex angle. It can be seen that within about 0.5mm from the nozzle, the expansion rate  $dA/dx$  is greater for the conical flow than for the free flow. Beyond that point, however, the expansion ratio of the free flow is substantially greater than for the conical flow for all stagnation pressures considered.

## AREA DISTRIBUTION ALONG STREAMTUBE

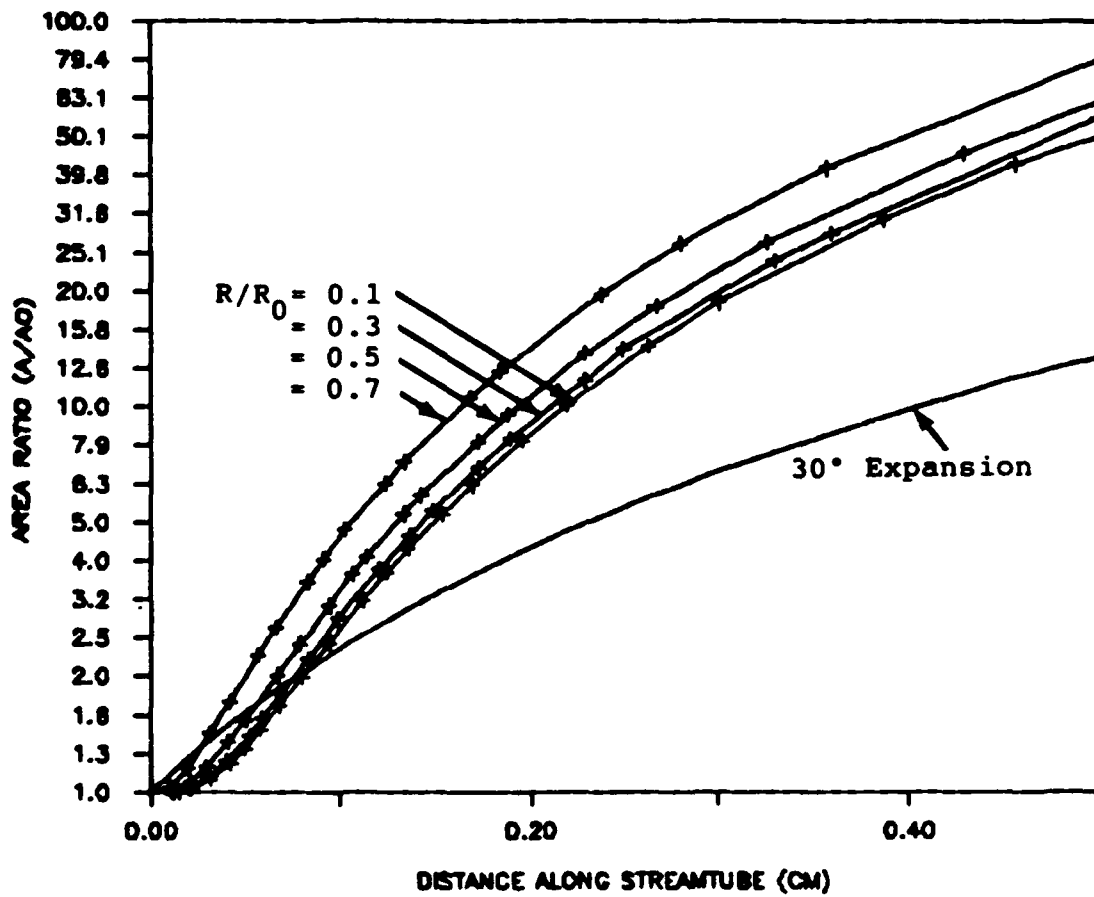


Figure 8. Areal expansion of streamtubes vs. initial radial starting distance from nozzle centerline.

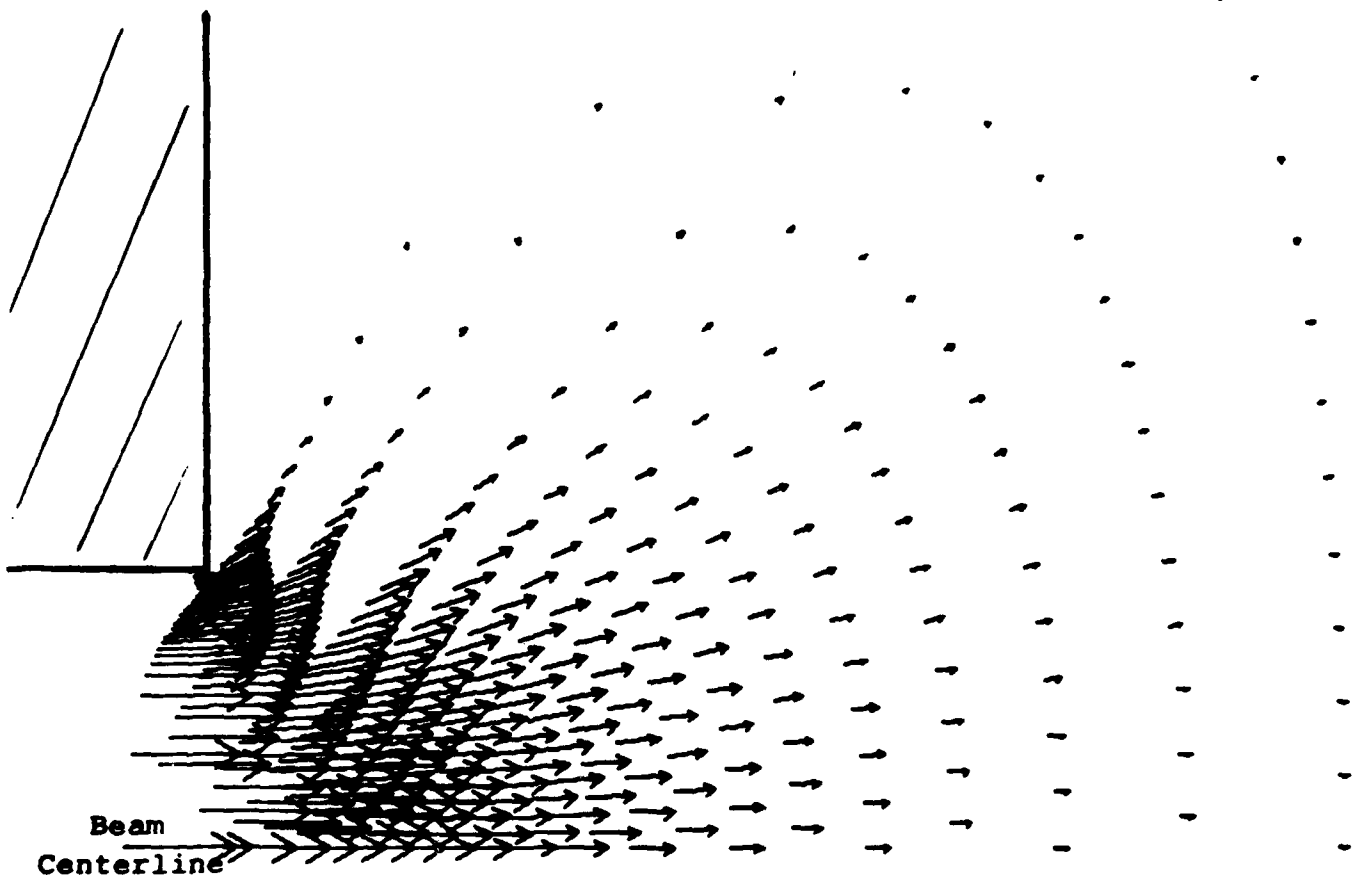


Figure 9. Distribution of mass flux in free nozzle expansion from 20 torr crucible.

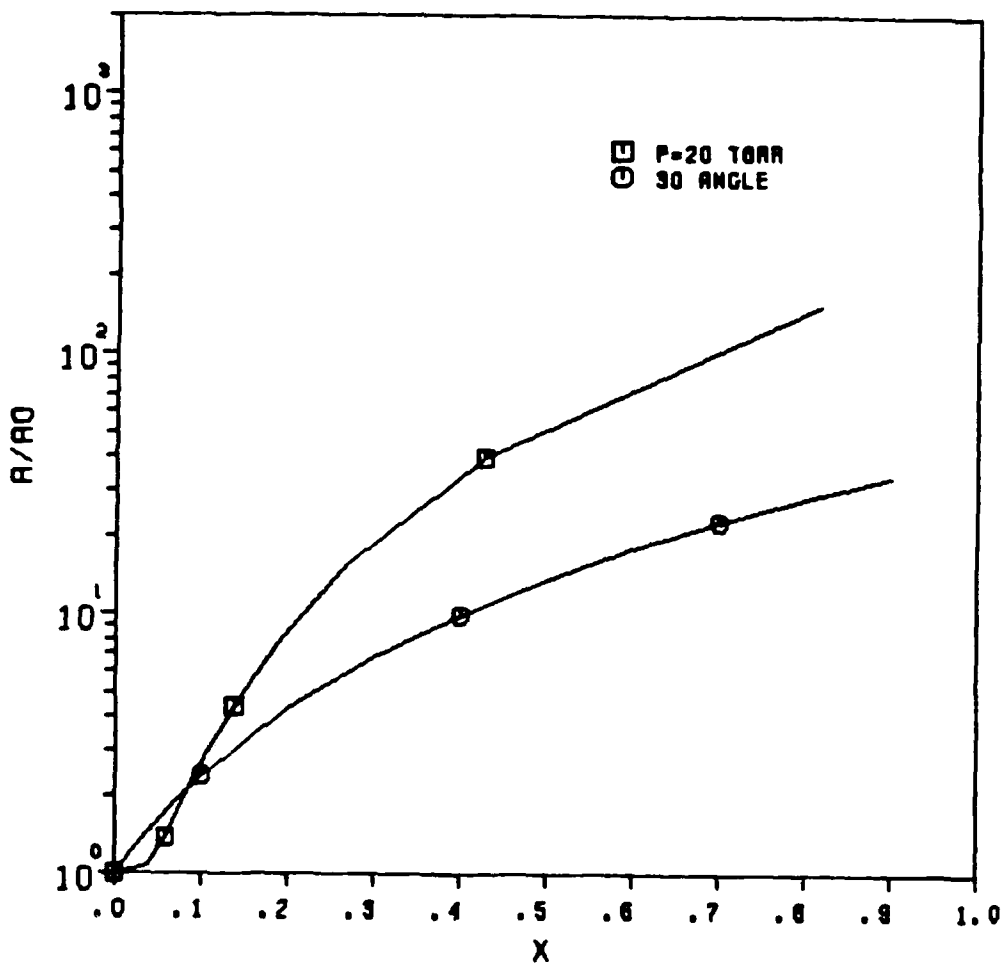


Figure 10. Beam expansion near centerline as calculated by characteristics method with  $P_0 = 20$  torr.  $30^\circ$  curve is expansion if uniform conical flow is assumed.

### 4.3 Results of Calculations

We chose aluminum as a working material in our numerical simulations because the experimental work was initially focused on aluminum vapor beams. Table I contains our primary results. In this Table under the heading "Flow" we have: flow through diverging nozzles, as studied by Hill; conical flow into  $30^\circ$ ; and free expanding flow calculated by the method of characteristics.  $P_0$  and  $T_0$  are the crucible stagnation pressure and temperature,  $d$  is the nozzle diameter, and  $\mu$  is the mass fraction of vapor which condenses into clusters. The last two columns,  $r_i$  and  $r_f$ , give the initial radius of clusters which nucleate at the throat and their final radius after reaching the end of the computational zone, respectively. Besides the cases listed, calculations were also performed for aluminum at  $P_0 = 1, 2, 5,$  and  $10$  torr, and for off-axis streamtubes. All of the cases shown are for flow near the beam axis.

In Figure 11, we present results for temperature (normalized to the stagnation value) as a function of the distance from the nozzle for the stagnation pressure  $P_0 = 20$  torr, the nozzle diameter  $d = 0.1$  cm, and a conical flow of  $30^\circ$  apex angle (run 3 in Table I). Here the lower curve corresponds to the isentropic expansion without condensation and the upper curve is from solution of equations (4)-(10) which include the effects of condensation. The conical flow case was run for comparison with the results of Usui et al. (1985) who assumed a simple  $30^\circ$  expansion.

The fact that the curves in Figure 11 do not coincide indicates that there is some condensation with latent heat release occurring. This fact alone, however, is not sufficient to draw the conclusion that clusters are growing. In Figure 12 we show the radius of the nucleating clusters at position  $x$ . It is assumed that the clusters begin with radius  $r_0(x) = 1.3r_c(x)$ . (The multiplier of 1.3 corresponds to a cluster size for which the growth probability is near 100%.) It can be seen that the critical radius decreases with  $x$  due to the lower vapor temperature. Also shown is a curve that gives the final radius of the clusters that originated at  $x$  and traveled to the end of the computational domain; the vertical displacement of the curves indicates the growth shown by a given cluster. Very clearly these results show that there was little cluster growth in run 3. The departure of the curve with condensation in Figure 11 from the isentropic one is therefore caused by the latent heat release due to the formation of a very large number of small nuclei, for which the condensation rate is only slightly greater than the evaporation rate. A similar conclusion is reached for run 4, where a larger orifice was assumed (0.2 cm). The beam temperature profile is shown in Figure 13 and droplet growth in Figure 14. The mass fraction  $\mu$  is somewhat higher as shown in Table I, in agreement with the general finding that high values of  $P_0 d$  lead to more condensation (Hagena, 1974). We should note that Usui et al. (1985) performed similar calculations for the same conditions, but in their paper the curve with condensation is removed further from the isentropic curve than in our case. Their results were thus more optimistic than ours. The reasons for this discrepancy are not known at the present time, since their paper states only final results without any discussion of the basic equations and the numerical method so that the comparison is difficult.

Table I. Examples of Numerical Simulation Results

Run	Material	Flow	Evaporation	$P_0$ (Torr)	$T_0$ [°K]	$d$ [cm]	$u$	$r_i$ (mm)	$r_f$ (mm)
1	H <sub>2</sub> O	nozzle	yes	490	374	-	0.054	0.6	5.5
2	H <sub>2</sub> O	nozzle	yes	490	400	-	0.037	1.6	1.76
3	Al	conical 30°	yes	20	2140	0.1	0.013	0.258	0.262
4	Al	conical 30°	yes	20	2140	0.2	0.027	0.241	0.247
5	Al	free	yes	20	2140	0.1	0.009	0.31	0.31
6	Al	conical 30°	no	20	2140	0.1	0.039	0.258	0.39
7	Al	conical 30°	no	20	2140	0.2	0.11	0.241	0.55
8	Al	free	no	20	2140	0.1	0.015	0.31	0.45

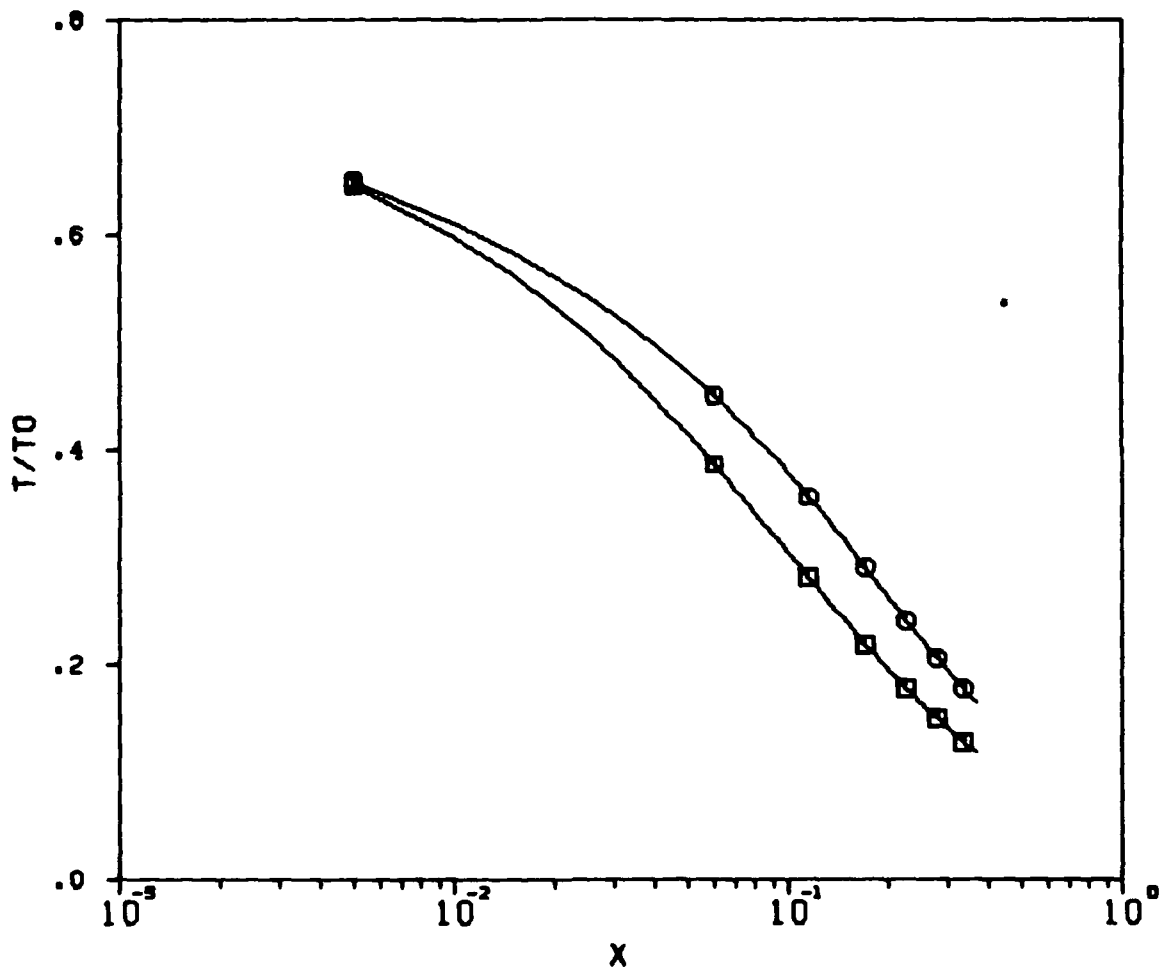


Figure 11. Calculated beam temperature vs. distance from 0.1 cm orifice nozzle. For aluminum in  $30^\circ$  expansion with  $P_0 = 20$  torr,  $T_0 = 2140K$ . Symbols are for curve labeling only: squares for isentropes, circles for condensing vapor.

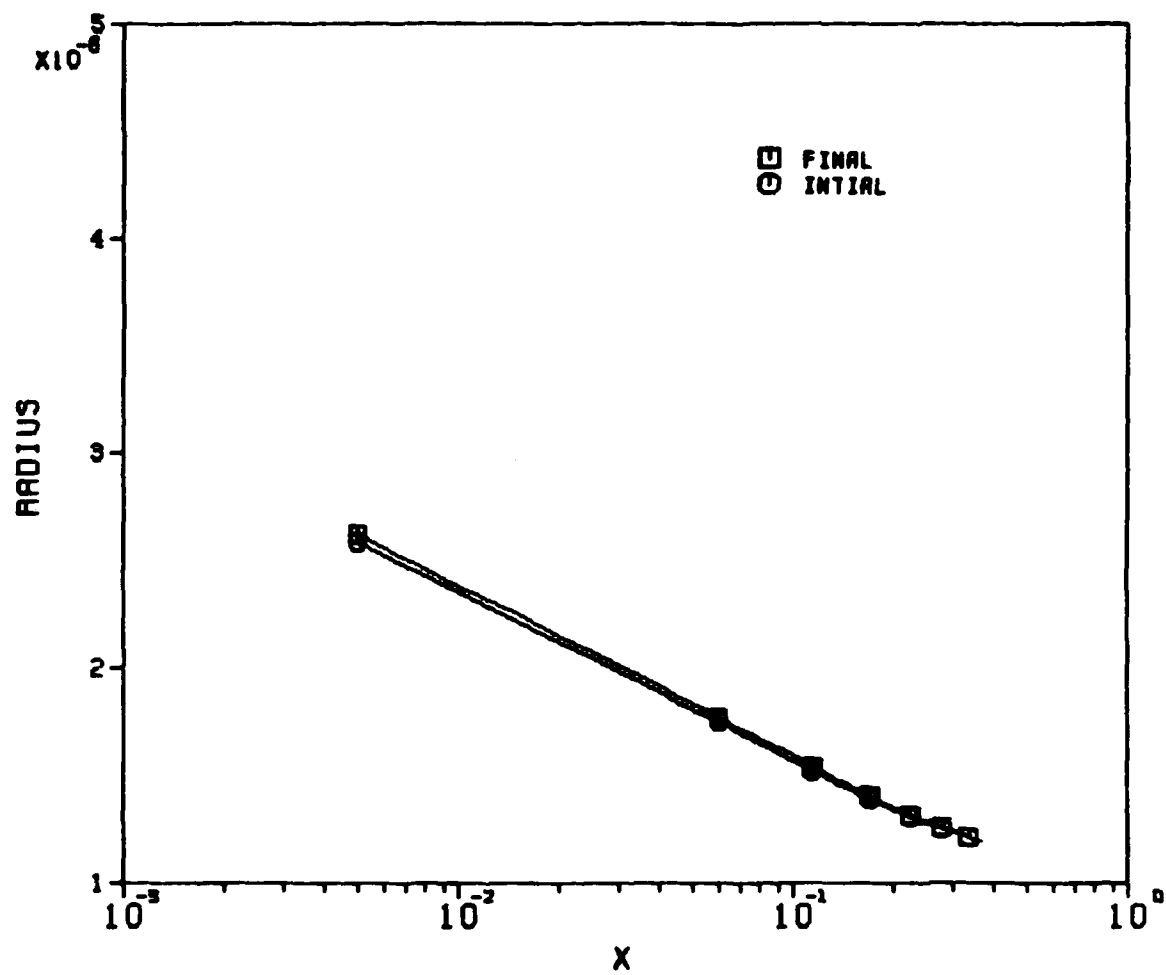


Figure 12. Cluster starting radius vs. position at which it nucleates (lower curve) and corresponding final radius (upper curve). For  $30^\circ$  expansion from  $P_0 = 20$  torr, 0.1 cm nozzle diameter.

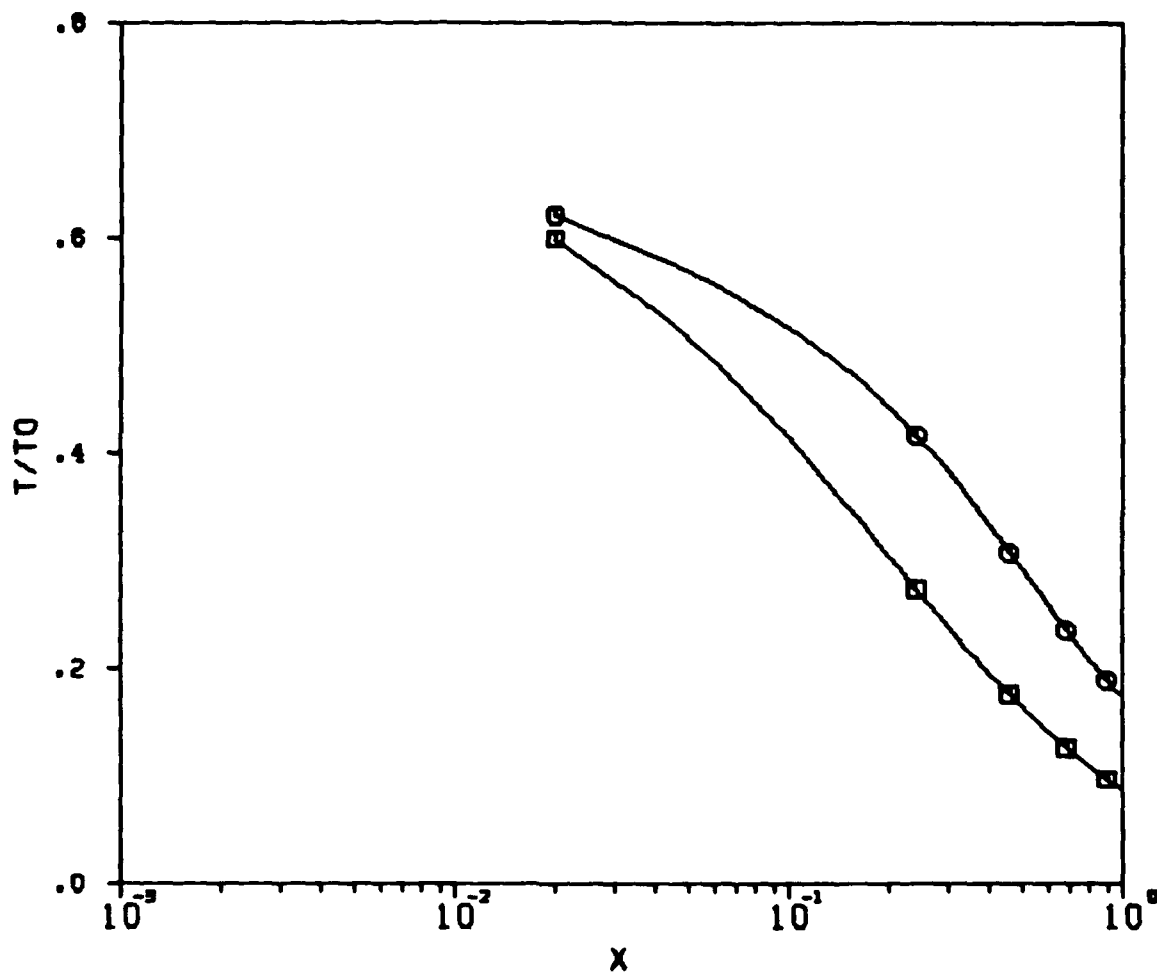


Figure 13. Calculated beam temperature vs. distance from 0.2 cm orifice nozzle. For aluminum in 30° expansion with  $P_0 = 20$  torr,  $T_0 = 2140K$ . Symbols are for curve labeling only: squares for isentropes, circles for condensing vapor.

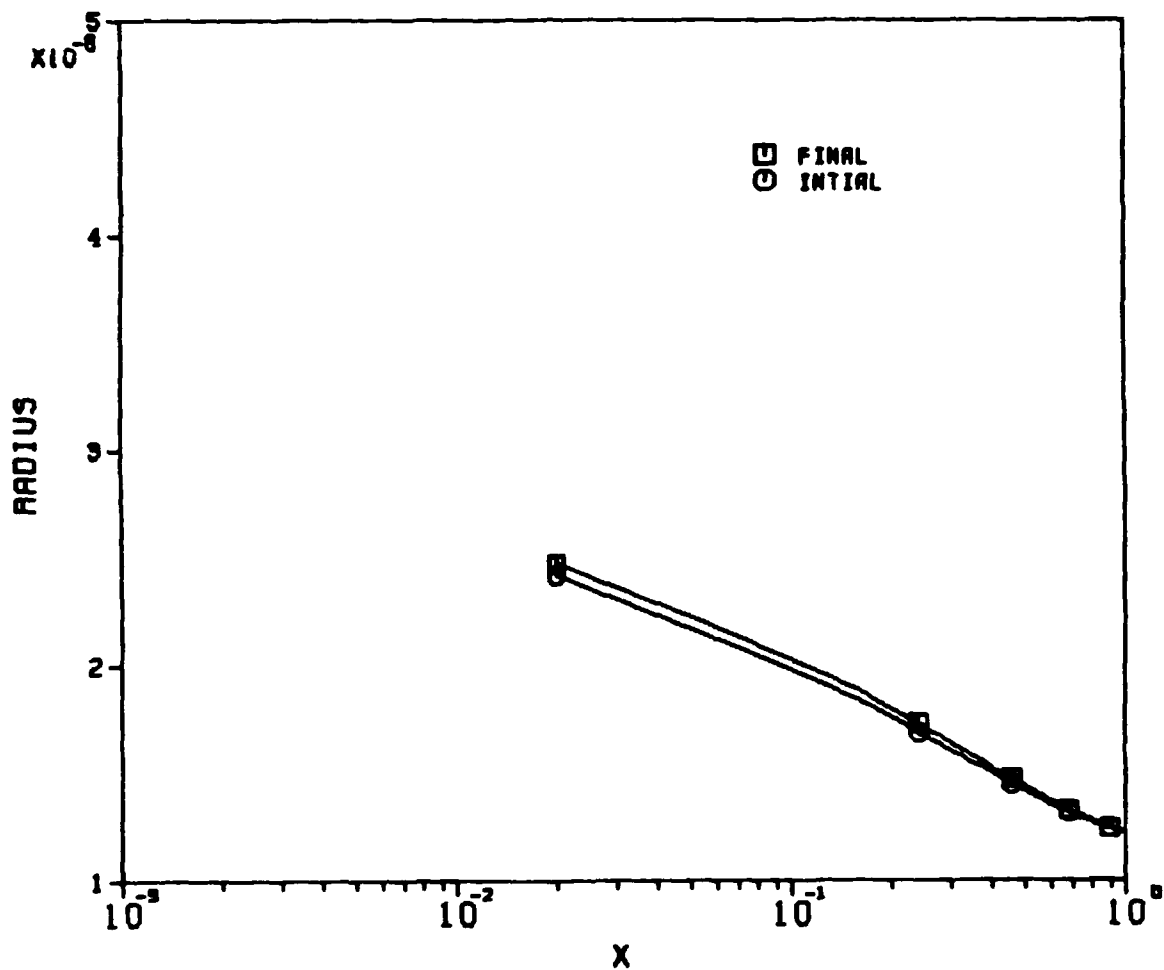


Figure 14. Cluster starting radius vs. position at which it nucleates (lower curve) and corresponding final radius (upper curve). For  $30^\circ$  expansion with  $P_0 = 20$  torr, 0.2 cm nozzle diameter.

Run 5 used area expansion ratios, calculated from the characteristics model rather than the  $30^\circ$  assumption. Temperature and cluster size are shown in Figures 15 and 16. Again, little or no growth occurred even though the nucleation rate was high. However, the condensed mass fraction dropped by 30% compared with case 3 ( $30^\circ$  expansion). In these runs, despite condensation reaching between 1 and 2% of the mass of the vapor (see Table 1) the radius growth is negligible. These cases should be contrasted with runs 1 and 2 for water vapor where the radius of the nucleating droplets grows by an order of magnitude in the condensation zone.

The relatively small radius growth rate can be explained on the basis of the following reasoning. An upper limit to the growth rate is found by setting  $\beta_D$  to zero, thus neglecting re-evaporation. The condensation rate (15) will have its maximum value just beyond the throat since the pressure decreases more rapidly than the square root of temperature. For  $P_0 = 20$  torr and  $T_0 = 2140^\circ\text{K}$  the maximum value of the growth rate computed for aluminum is  $dr/dt = 0.04$  cm/s. The velocity of the clusters is comparable to the velocity of sound at the throat which from (20) is  $c = 9 \times 10^4$  cm/s. Therefore, under the most favorable conditions, one may expect clusters to grow from  $r_i = 0.3$  nm to  $r_f = 1.6$  nm (1000 Al atoms) in a distance of 0.33 cm. In reality,  $dr/dt$  will decrease with distance so that the condensation zone is always much less than 1 cm; the maximum growth rate cannot be sustained over a distance much greater than about one nozzle diameter (0.1 cm in this example). Nucleating droplets probably do not grow by more than about 0.4 nm even with evaporation neglected, yielding clusters of perhaps 90 atoms.

To confirm these estimates, we have rerun cases 3-5 with  $\beta_D$  set to zero in our program (runs 6-8). Results are shown in Figures 16-22. The total amount of condensed phase increases if evaporation is neglected, but even then the radius increase does not exceed 0.3 nm. To be more exact, the largest radius achieved in our simulations is 0.55 nm which corresponds to a cluster consisting of 42 aluminum atoms at bulk density. This is consistent with experimental results reported by Kuiper (1981) for silver beams.

#### 4.4 Limitations of Model

Since in Takagi's experiments clusters consisting of 500-1000 molecules are reported, it is worth discussing possible limitations in our modeling that could lead to overly pessimistic results. Probably the weakest point in our calculations is the assumption that the vapor nucleates at a point  $x$  with a monochromatic spectrum of droplets of radius  $1.3r_c$ . If these droplets grow very rapidly as in the case of water vapor in a supersonic nozzle, this assumption is not important since the size of the droplets after passing the condensation zone is to a large extent independent of the initial size (before entering the condensation zone). In reality, however, the nucleation process creates an entire spectrum of drop sizes which may be determined from the Gibbs distribution. If they grow only very little, the final distribution of sizes may depend strongly on the initial distribution. Moreover, since larger droplets grow faster (the growth in volume is proportional to  $4\pi r^2 dr/dt$ ) the presence of larger droplets in the initial distribution could lead to a prediction of much larger clusters.

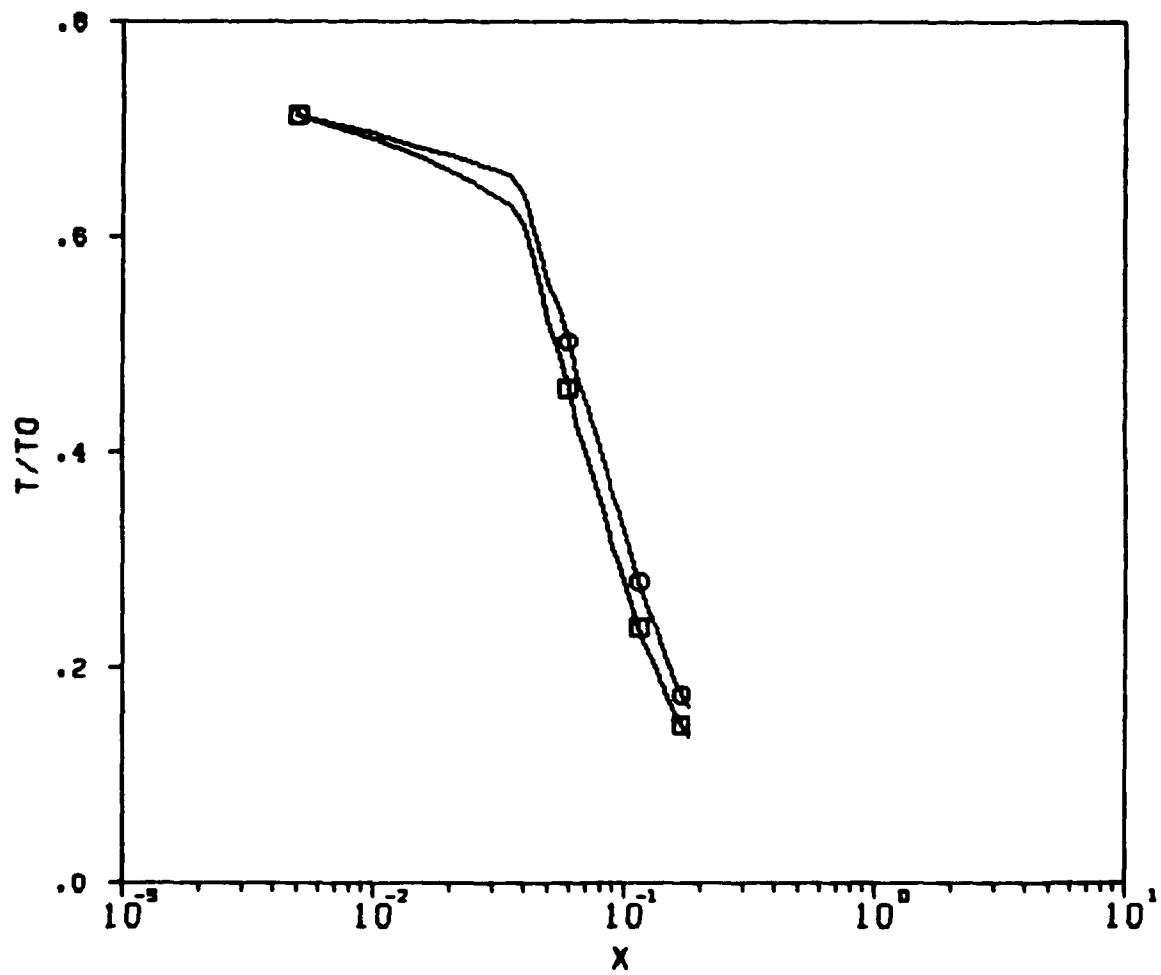


Figure 15. Calculated beam temperature vs. distance from 0.1 cm orifice nozzle. For aluminum by method of characteristics with  $P_0 = 20$  torr,  $T_0 = 2140K$ . Symbols are for curve labeling only: squares for isentropic, circles for condensing vapor.

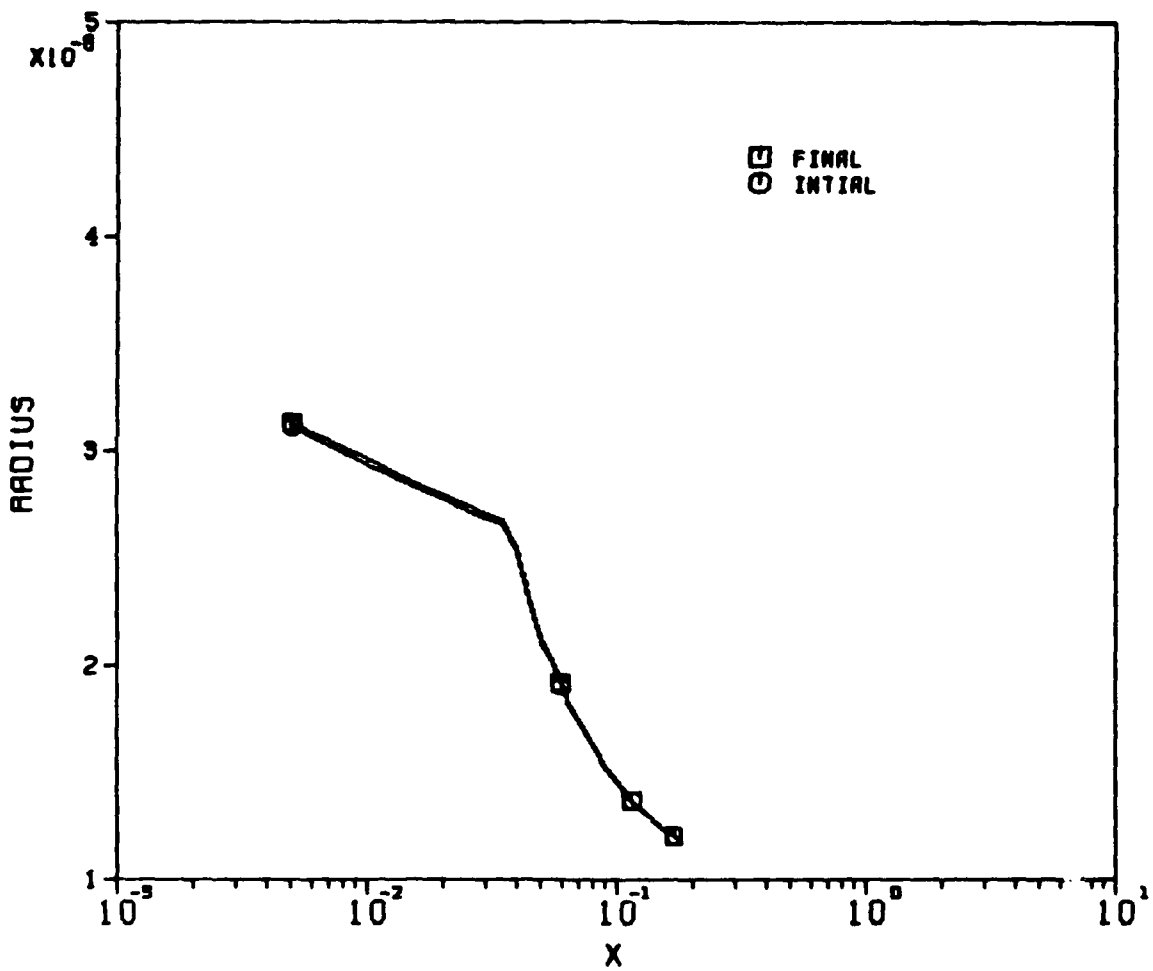


Figure 16. Cluster starting radius vs. position at which it nucleates (lower curve) and corresponding final radius (upper curve). By method of characteristics with  $P_0 = 20$  torr, 0.1 cm nozzle diameter.

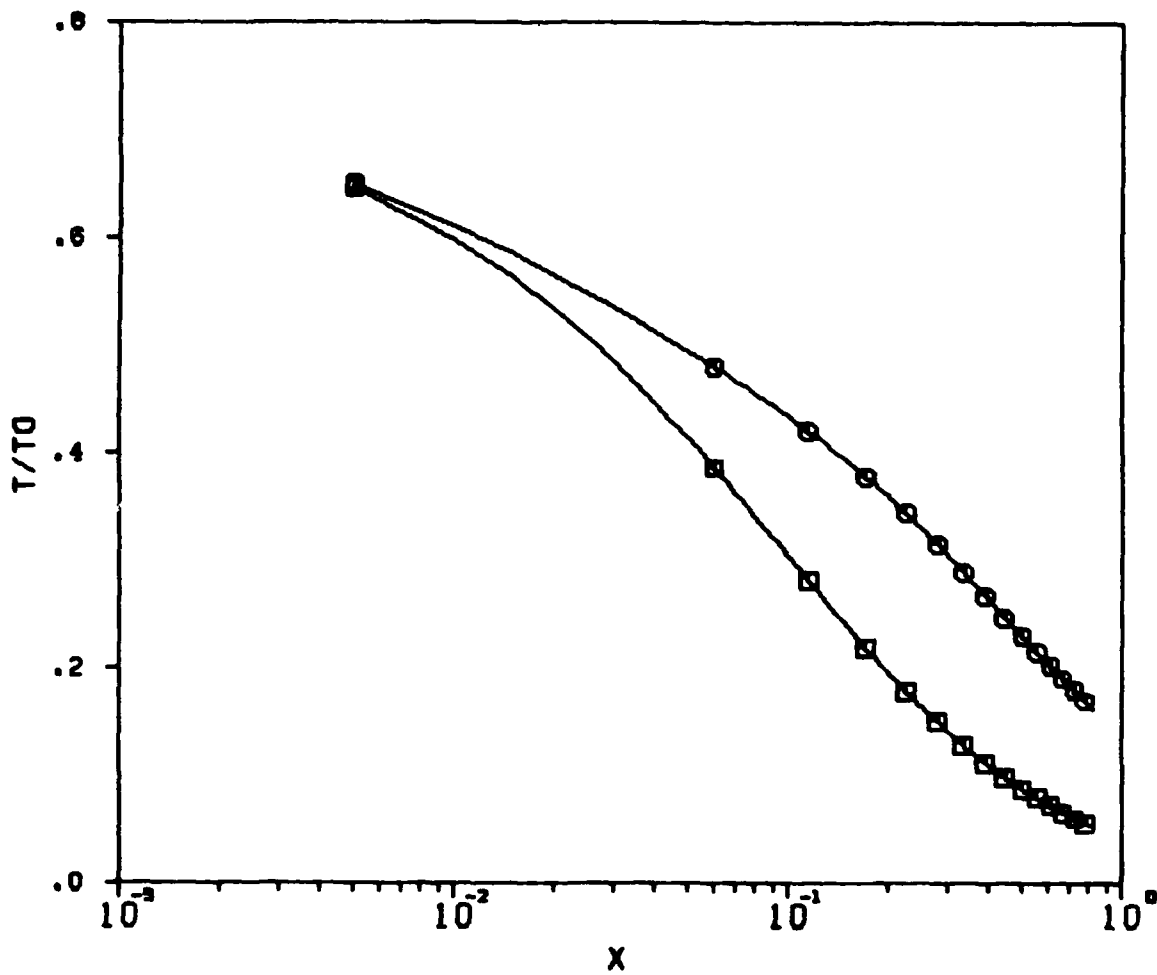


Figure 17. Beam temperature for Run 6 (evaporation disallowed).

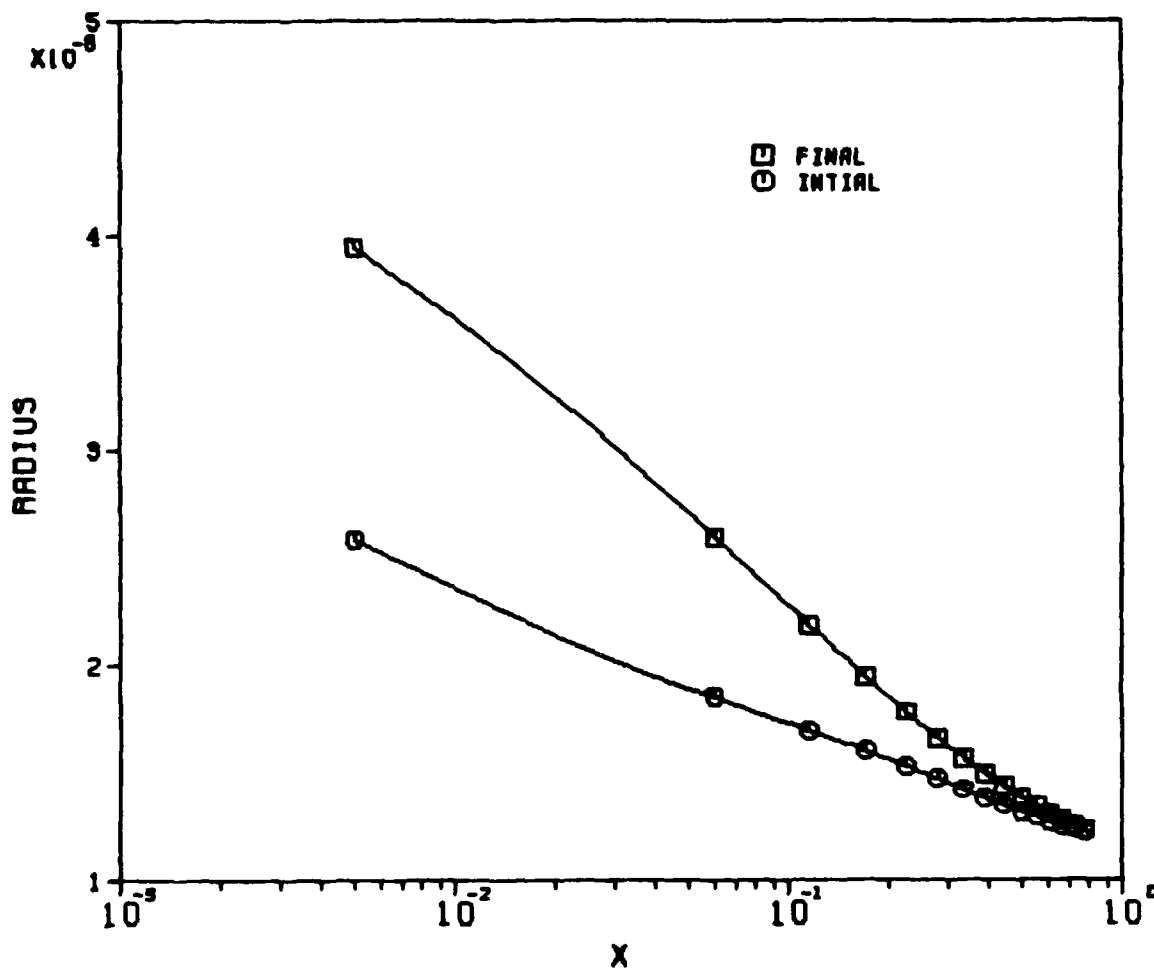


Figure 18. Cluster initial and final radius vs. nucleation position for Run 6 (evaporation disallowed).

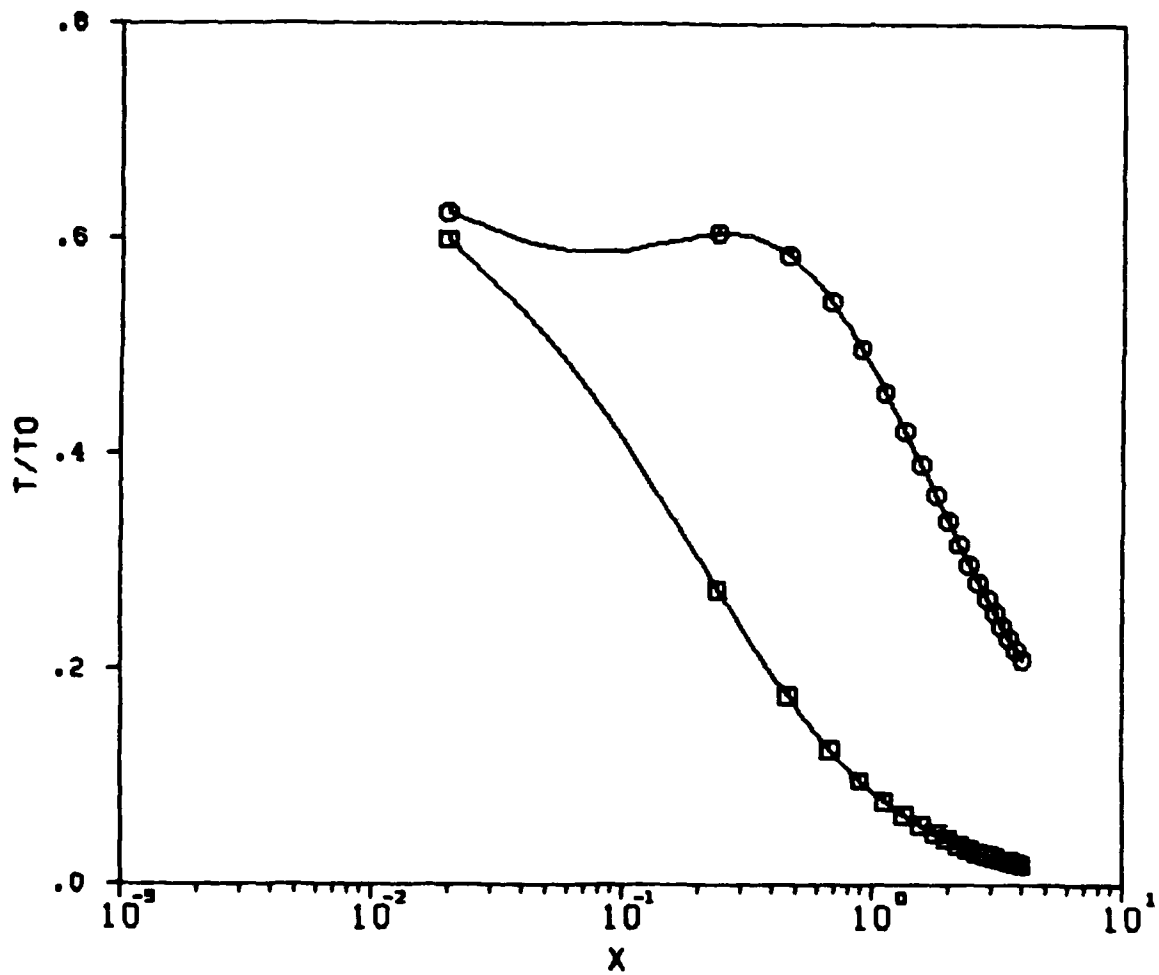


Figure 19. Beam temperature for Run 7  
(evaporation disallowed).

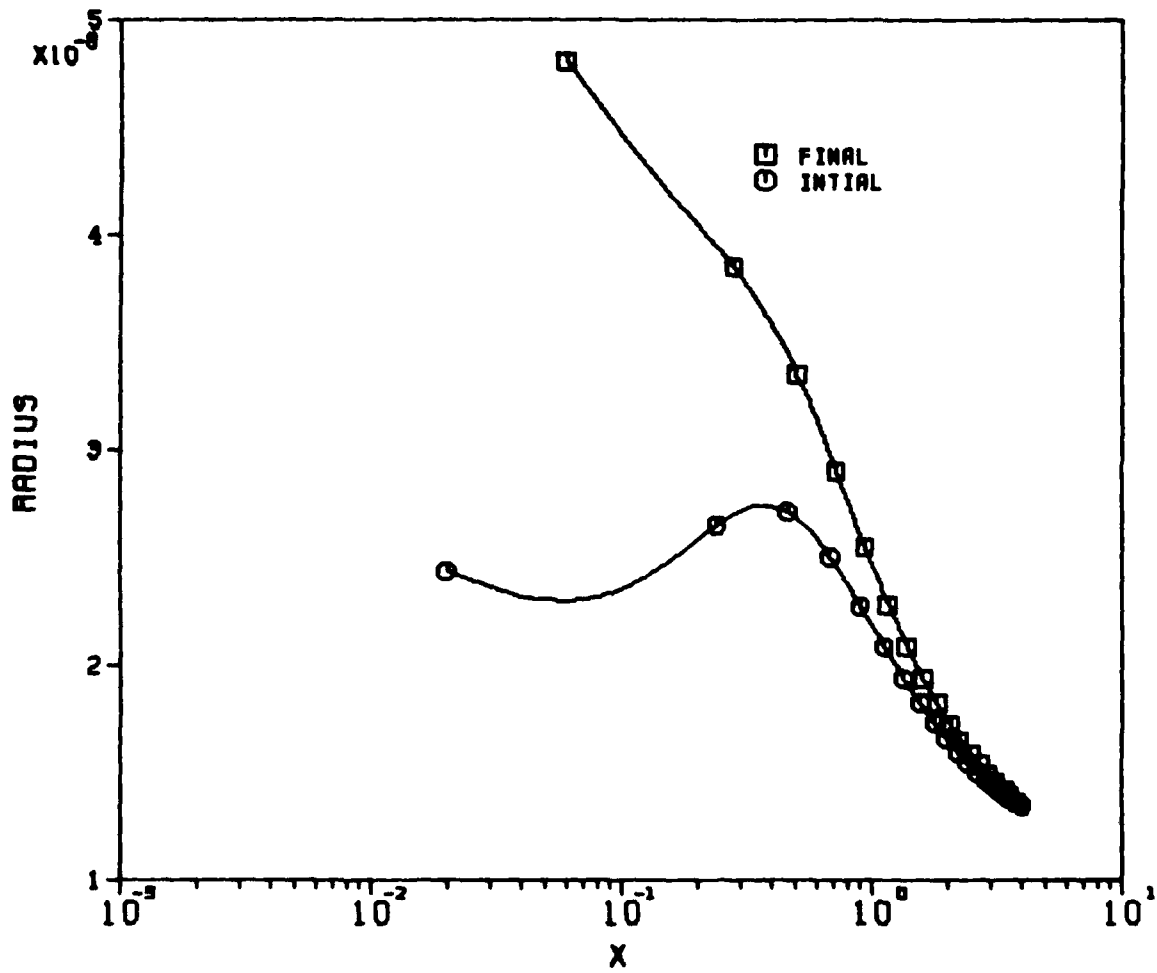


Figure 20. Cluster initial and final radius vs. nucleation position for Run 7 (evaporation disallowed).

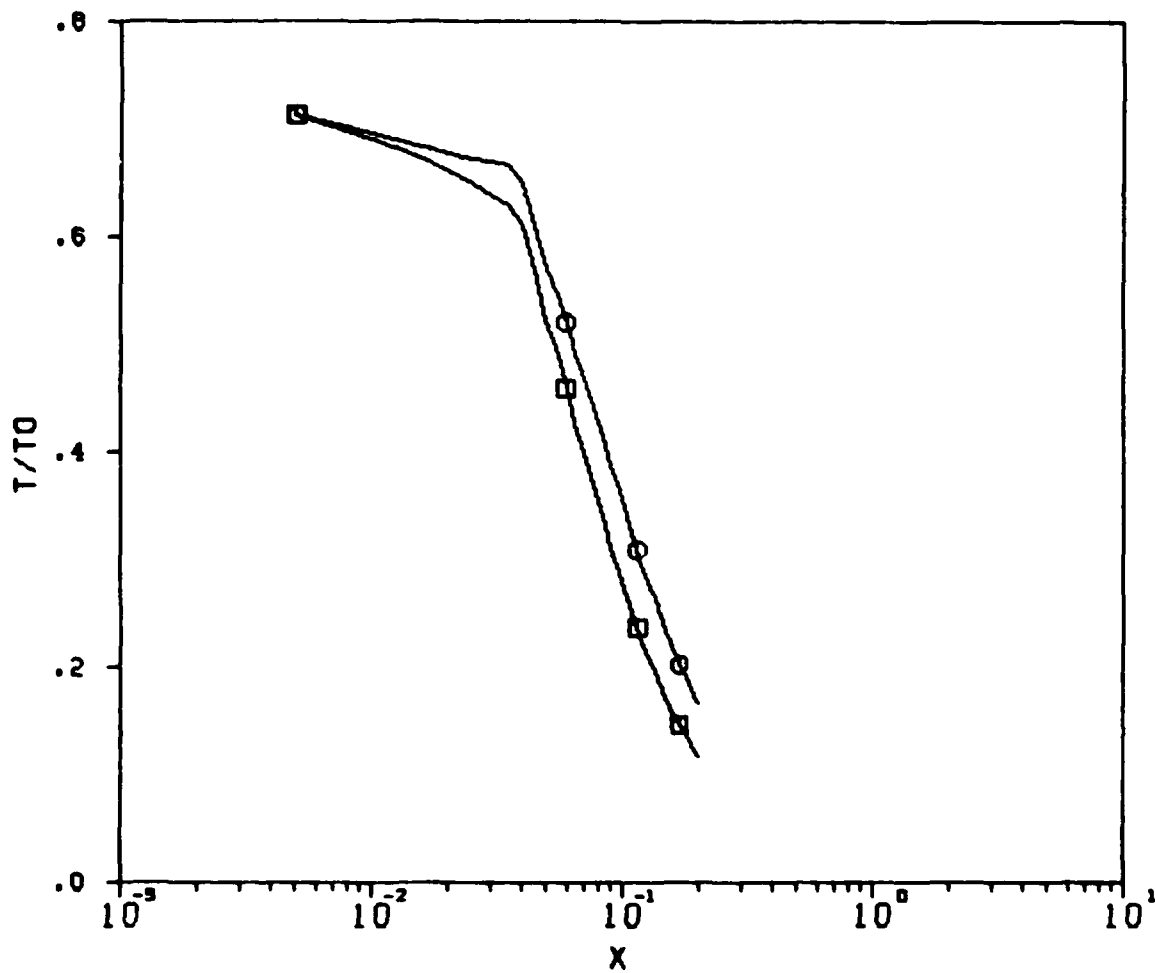


Figure 21. Beam temperature for Run 8  
(evaporation disallowed).

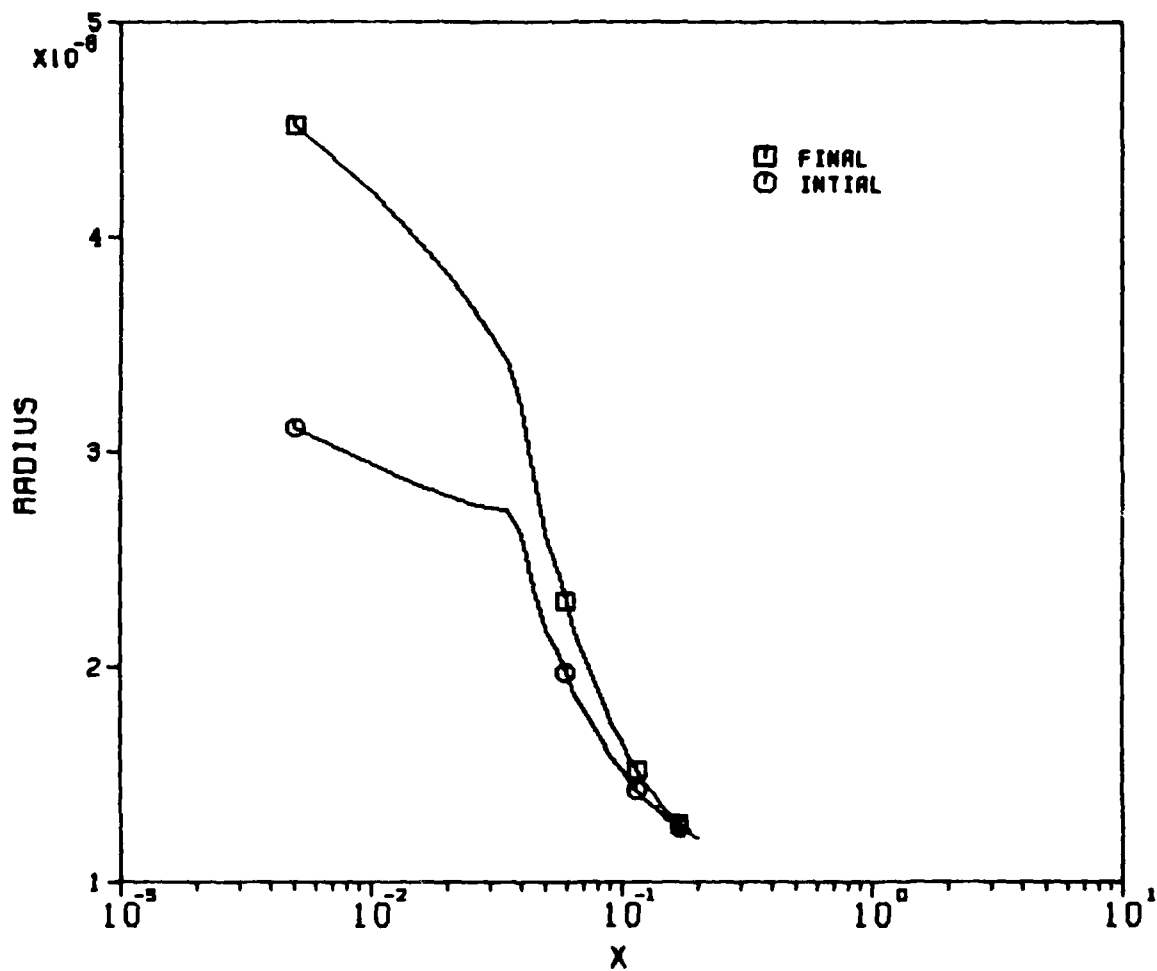


Figure 22. Cluster initial and final radius vs. nucleation position for Run 9 (evaporation disallowed).

Another drawback of our approach is the use of the conventional steady state nucleation theory. Since the jet expansion is very rapid, it is probably preferable to use a non-steady theory, following the evolution of the entire spectrum of drop sizes and solving the kinetic equations for condensation and evaporation (Yang & Lu, 1986).

We have also considered the possibility of cluster coalescence to explain the presence of large clusters. This explanation appears unlikely since the estimated mean free path for clusters at  $P_0 = 20$  torr and  $T_0 = 2140^\circ\text{K}$  is over 100 cm. This figure was arrived at by considering the cross-sectional area and number density of nuclei when the mass fraction  $\mu = 0.01$  as in case 5 of Table I. Even if  $\mu = .1$ , the mean free path would be much too long to give a substantial amount of coagulation growth.

Radiative cooling of small clusters might also be important in determining their temperatures, and therefore their ability to pass off excess heat of condensation. To our knowledge, this possibility has not been considered elsewhere, and did not occur to us until the modeling work was largely completed. However, it is certainly plausible that the high temperatures of the particles combined with their high surface to volume ratio could lead to some significant degree of cooling. The cooling rate due to thermal radiation is

$$\frac{dT}{dt} = - \frac{\epsilon A \sigma T^4}{m c_p}$$

where  $\epsilon$  is the emissivity,  $A$  the surface area,  $\sigma$  the Steffan-Boltzmann constant,  $m$  the mass, and  $c_p$  the specific heat. This can be integrated to give the temperature as a function of time:

$$T = (1/T_0^3 + 9\epsilon\sigma/\rho r c_p)^{-1/3}$$

As an example, we calculated the temperature of a 100 atom aluminum cluster ( $r = 0.8$  nm) which is initially at 2100 K. If it is assumed that  $\epsilon = 0.1$ , then the cluster will cool to 1798 K in  $10^{-5}$  seconds. In the nozzle flow of an expanding jet this represents about 2.5 mm of travel, comparable to the size of the condensation zone. Such high cooling rates could not only release the heat of condensation but may act as a sink for the vapor as a whole, increasing the superaturation level.

A difficulty arises in trying to apply this model in a realistic way because the emissivities are unknown. The emissivity of a metal is closely related to its reflectance, which is in turn a function of the dielectric constant. Ordinarily metals have low emissivities (less than 0.1) and are poor radiators. However, Kreibig and Fragstein (1969) modeled the optical properties of silver particles and found that the refractive index should increase dramatically for particles smaller than the mean free path of

conduction electrons in the metal. Using their model we calculated that a silver sphere of 1 nm radius will have a reflectance of about 0.59, as compared with 0.96 for bulk silver, at a wavelength of 400 nm. This suggests an emissivity of about 0.4, leading to even more rapid cooling than the example of the paragraph above. Other complicating factors such as wavelength and temperature dependence and relaxation times ought to be considered in a complete treatment of radiative cooling, but our estimates show that it is a potentially important mechanism.

#### 4.5 Other Mechanisms for Cluster Growth

An alternative mechanism for cluster formation and growth has been proposed by Knauer (1986, 1987). It postulates that nuclei grow heterogeneously on interior surfaces of the crucible, then detach and are entrained in the vapor flow through the nozzle. This mechanism has two advantages over the homogeneous model: first, the substrate can take up some or all of the heat of condensation of the metal vapor; and second, it should be easier for atoms to nucleate in a two-dimensional space than in three dimensions.

In Knauer's model, surface nucleation and growth rates are calculated for metal vapor which arrives at a high flux on a surface slightly cooler than the rest of the crucible. This could be the walls of the nozzle or nearby interior surfaces. If the surface is much cooler (more than 15°C) or if the clusters form strong bonds to the surface, they will continue to grow until a continuous layer is formed. However, if the bonding is weak, high energy phonons can eject clusters in balance with the nucleation rate. A number of assumptions regarding the energies of attachment and diffusion of atoms and the bonding energy to the surface had to be made in Knauer's paper; however, he was able to predict that silver clusters of about 600 atoms ought to be producible in reasonable numbers within a narrow range of conditions.

The conditions are in fact very narrow and difficult to establish or measure. Figure 23 shows some results of Knauer's calculations which indicate how closely the temperature differences must be controlled. A key condition is that the metal vapor should not wet the crucible material; on a macroscopic scale this is easy to establish, but not so straightforward for aggregates of a few tens or hundreds of atoms on a rough surface. It is also quite difficult to measure crucible temperature profiles accurately enough in the temperature range required.

As will be discussed later, we performed numerous experiments to try to establish the prescribed conditions and did not find evidence of clusters in the 600 atom range. Another group working at Sohio (Windischmann, 1987) obtained a similar result. However, we did find larger particles issuing from the orifice, and were able to correlate their presence with crucible surface processes by studying wall deposits on rapidly cooled crucibles. We therefore regard the heterogeneous growth explanation to be unproven but quite plausible.

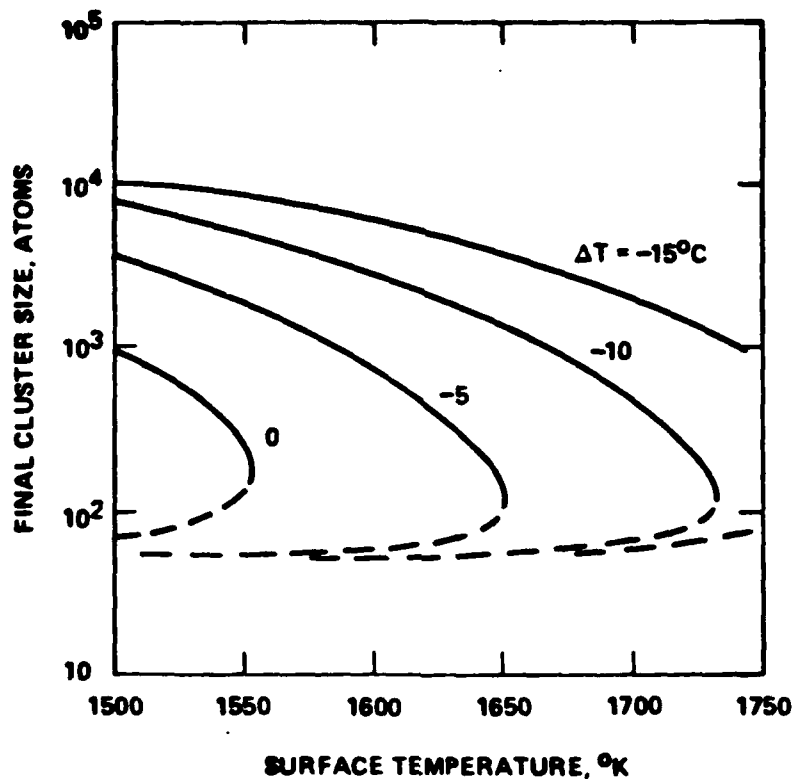


Figure 23. Cluster size vs. crucible temperature differential, from heterogeneous theory (From Knauer, 1987).

## 5.0 EXPERIMENTAL DEVELOPMENT

### 5.1 Initial Assumptions

At the outset of the Phase I investigation we acted upon several assumptions which guided our approach. The most important was that cluster formation could occur in a pure metal vapor expansion, using the type of nozzled crucible described by Takagi (1975, 1984). This assumption appeared reasonable based on some if not all of the evidences which Takagi's group published in a long series of papers, as well as private and group discussions held with members of his research team. Credible evidence of large clusters has recently appeared from other sources (Knauer, 1987) so that this assumption is not seriously doubted.

A second assumption was that the homogeneous nucleation and growth mechanism proposed by Takagi was essentially correct. This mechanism is known to account for the growth of water and rare gas clusters in supersonic expansions. Also, calculations had recently been published (Usui, 1985) which predicted sufficiently high nucleation rates for metal vapors. If this second assumption were true then it should have been possible to produce clusters in the size range which has been reported; Takagi's papers give the dimensions of the nozzles and the crucible stagnation pressures at which clusters appeared. Surface properties would then play no part. We planned to make our major contribution by substantially improving beam characterization techniques and then using these in the course of a scientifically based thin film development program.

Our equipment was built in-house, which allowed us to quickly bypass many of the problems which other U.S. investigators were experiencing with commercial systems. As a result we were able to successfully test the basic Takagi crucible configuration using a well-characterized analysis and detection system. Because of the very low upper limit which was then placed on cluster population, the assumption of homogeneous growth was set aside in favor of the surface growth mechanism. However, we were then faced with a greater challenge because of the much greater difficulties involved in independently measuring and controlling a multi-temperature crucible. The crucible material and surface condition also became a concern at that point.

A third assumption was that clusters in the supersonic beam should have nearly the same velocity as the monomers. This implies that their kinetic energies will be proportional to their masses, so that energy analysis can be used to obtain a mass distribution. At the temperatures of interest, monomers accelerated in a nozzle expansion will have an average translational energy  $E = 5/2 kT = 0.35\text{eV}$ . If  $N = 1000$  atoms are collectively accelerated before condensing, the cluster should have  $E = 5/2 NkT = 350\text{ eV}$ . This method is not as accurate as quadrupole analysis but has been shown to give good agreement in a wide range of experiments with rare gas clusters and seeded beams. It was used by Yamada for silver clusters; typical data are shown in Figure 24. If instead clusters are formed on crucible surfaces and detach, they must be accelerated by drag forces and may not achieve the monomer velocity. However, we have performed drag calculations which show that 1000 atom clusters should reach 97% of the monomer velocity while traversing a 1 mm path through a nozzle.

Arrangements have been made with the Microelectronics Center at Iowa State University to do time-of-flight mass spectrometry when appropriate, to verify and refine the mass distributions from our cluster sources. The time-of-flight apparatus was not completed within the contract period, but may be useful in our future work.

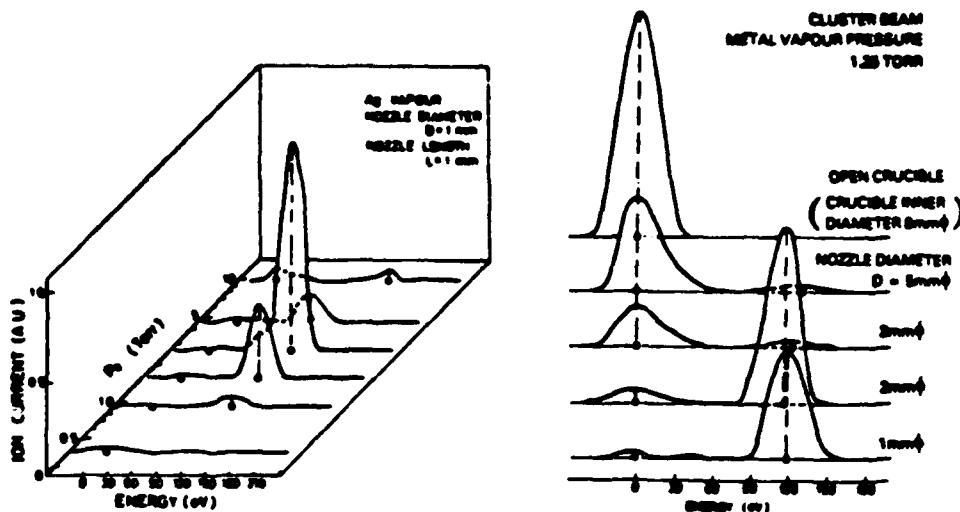


Figure 24. Electrostatic energy analysis of silver cluster beam (from Yamada, 1981).

## 5.2 Initial Hardware Design

A ground-up approach was taken in developing the experimental apparatus, which avoided any artifacts or difficulties associated with ICB equipment supplied commercially. The principal investigator also had the benefit of experience in design of ICB components from earlier work. A schematic diagram of our source apparatus is shown in Figure 25, and a photograph in Figure 26.

The work was carried out in an Enerjet UCV 18/6 diffusion pumped system, shown in Figure 27. Special care was taken to keep chamber pressures below  $10^{-6}$  torr during the experiments to reduce spurious ion signals due to background gases. A residual gas analyzer was used to monitor actual chamber gas pressures and composition.

Resistance heating was used for the crucibles. This was much simpler than the electron bombardment heating used by Takagi, and kept stray electron or ion currents to a minimum in the chamber. Initially, boron nitride crucibles were used instead of graphite because BN is not attacked by aluminum. Crucibles were machined to fit in commercially available crucible heaters; the lids were made separately and in early versions simply rested on the crucible body. Extra heat shielding was added to improve temperature uniformity. A typical crucible is shown in Figure 28. Thermocouple and pyrometer measurements, and modeling of radiative heat losses from the lid, determined that the lid was about  $60^{\circ}\text{C}$  cooler than the body of the crucible. The lid orifice had a 1 mm diameter and both cylindrical and conical profiles were tried.

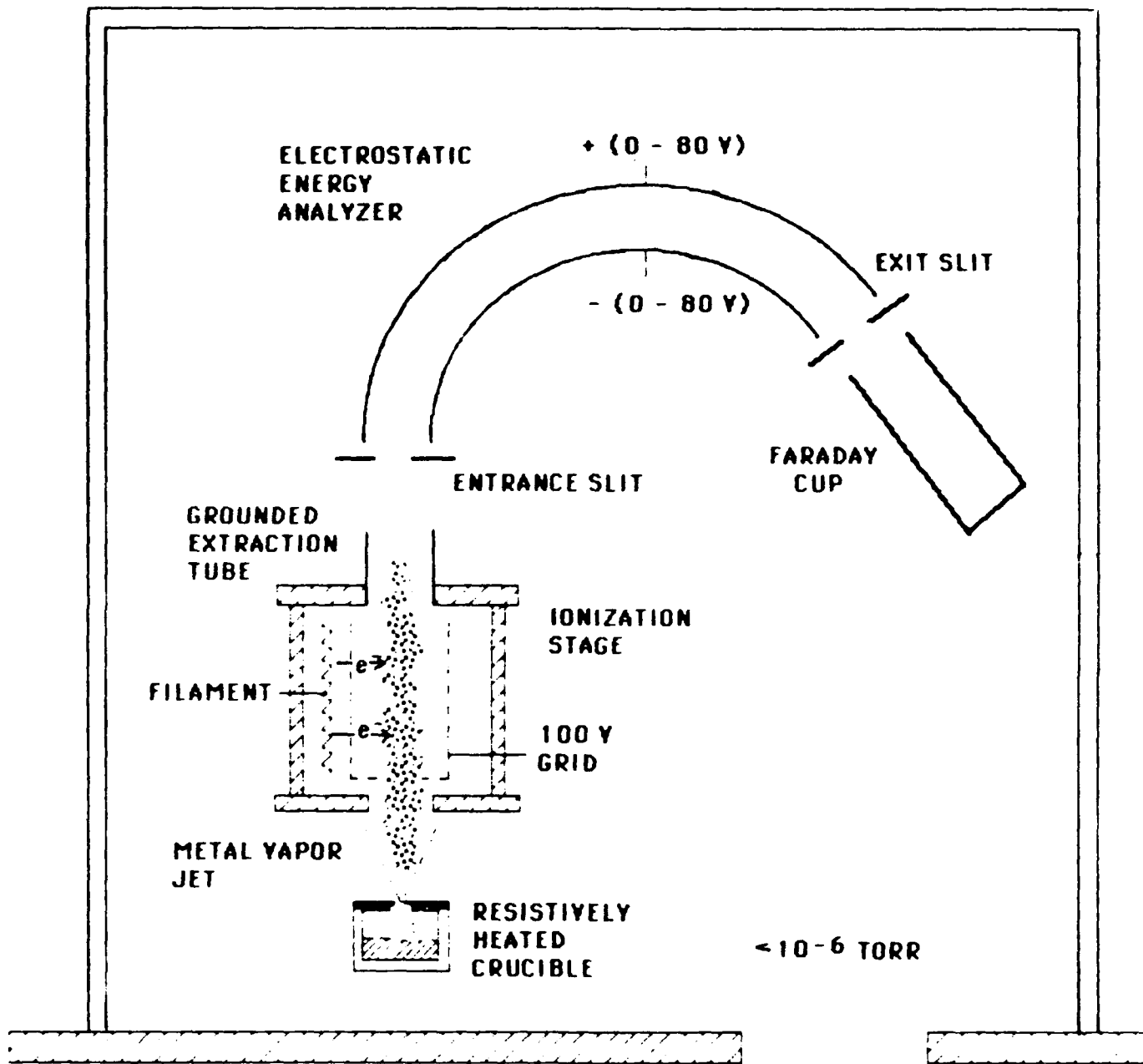


Figure 25. Schematic diagram of apparatus.

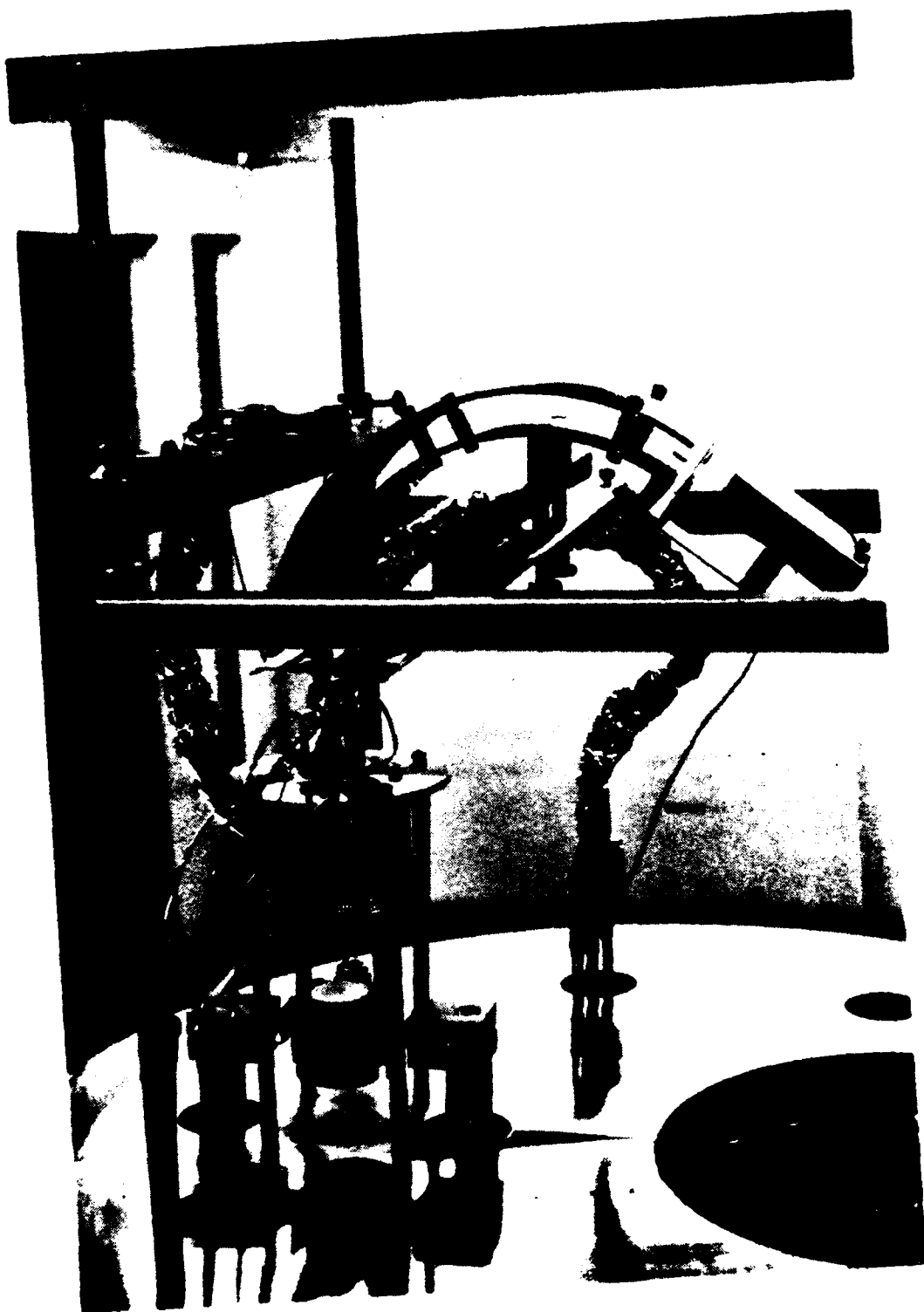


Figure 26. Cluster beam source, ionizer, and detectors.

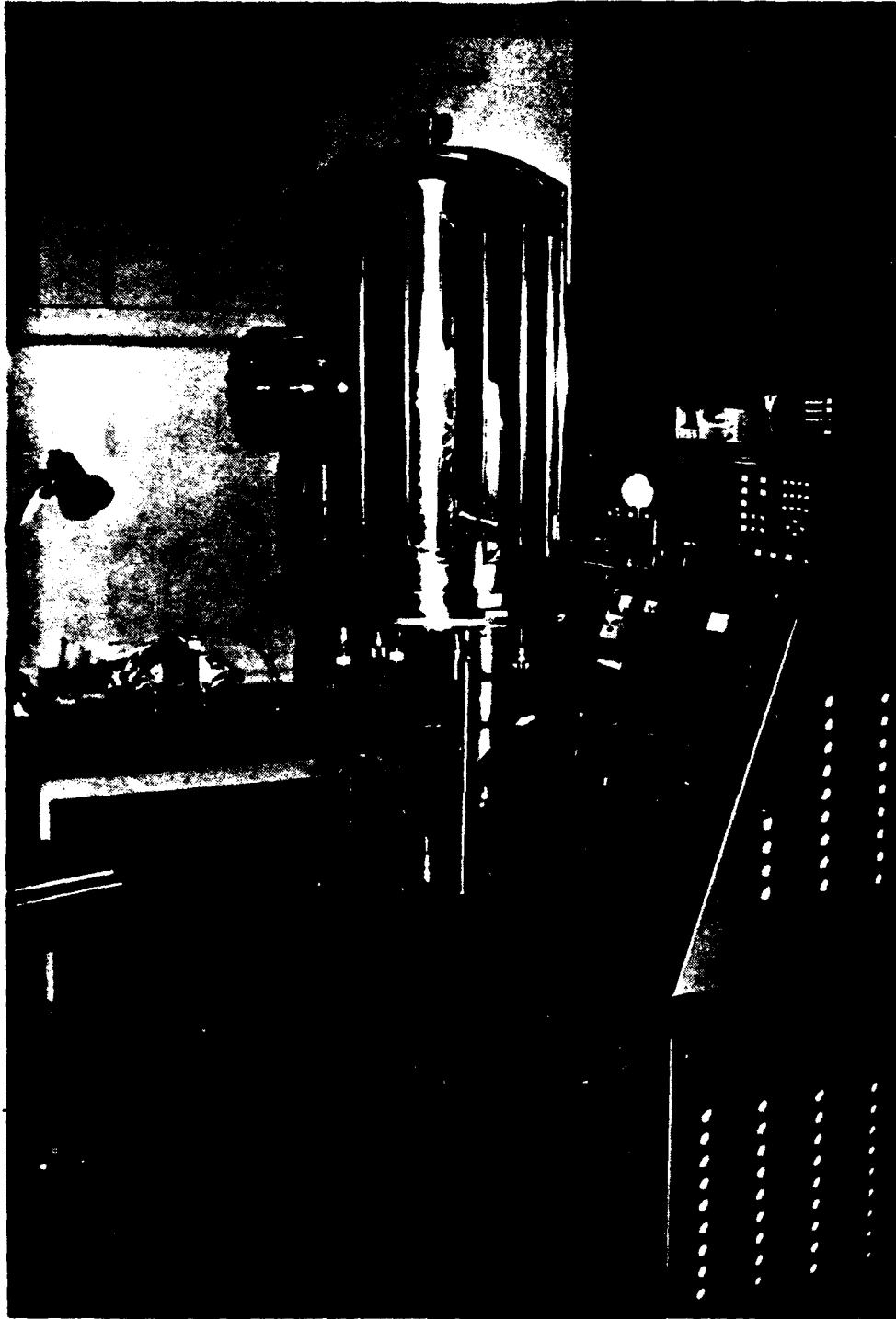


Figure 27. High vacuum chamber for Phase I cluster beam study.



Figure 28. Boron nitride crucible in heater.

The electron impact ionizer is shown partially disassembled in Figure 29. It includes the grid and filament from a conventional ionization gauge. This made construction easy and had the advantage that its ionization efficiency is known or can be calculated for various gases and metal vapors. Because the electrons can make several passes through the beam ionization region before being intercepted by an atom or collected by the grid, it is most important that ionizers of this type be calibrated. One of the difficulties in interpreting Takagi's results is that no such calibration is ever given, only measurements of the total grid current. He also used a non-standard grid configuration, which makes it virtually impossible to even guess at the actual electron current densities. The characterization of our ionizer will be discussed in Section 5.3.2.

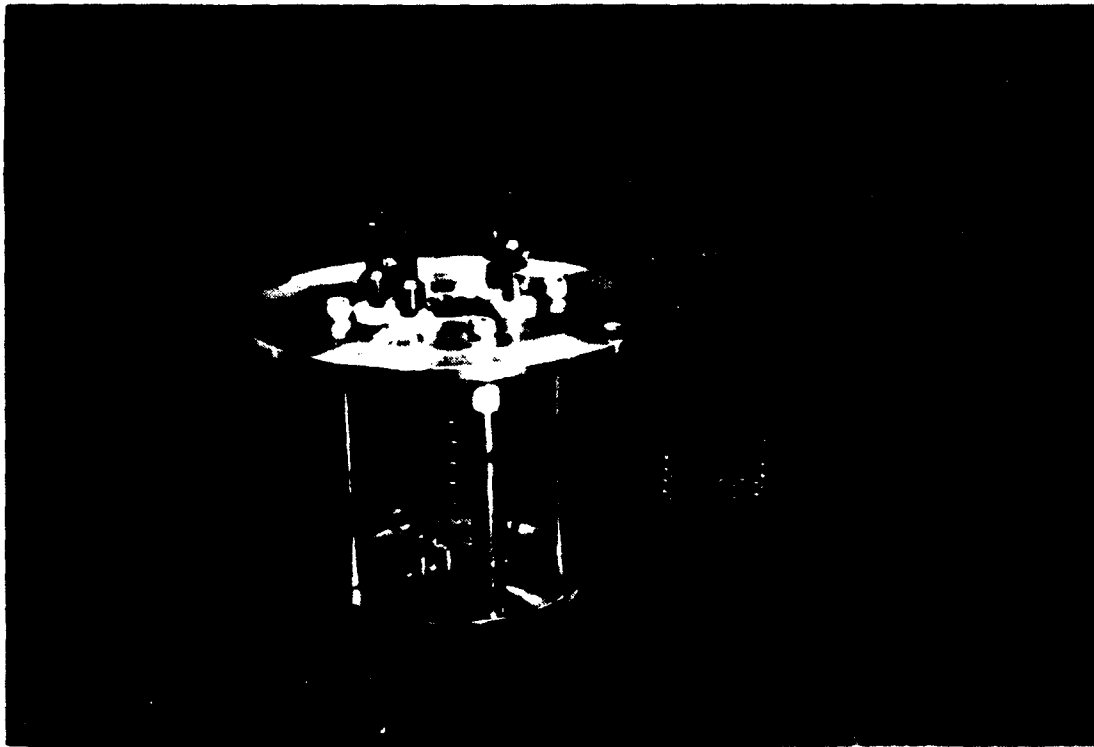


Figure 29. Ionization stage with screen removed.

A key requirement which we placed on the ionization stage was that it should efficiently transmit all species in the beam. Transmission is not a problem for massive clusters which obtain roughly 300 eV of kinetic energy from the nozzle expansion. However, monomers which enter the ionizer with 0.3 eV before ionization will be at the mercy of small field gradients once they are charged. Only by extracting all ions could we hope to obtain a quantitative sampling of the beam constituents.

To meet the efficiency requirement, the top plate of the ionizer was electrically isolated from the filament and grid so that an ion extraction potential could be placed on it. Typically, the grid was maintained at 75 to 100 volts and the ions accelerated toward a grounded plate. Extraction of an ionized beam was problematic at first with the open cylindrical grid. The ion currents passed to the Faraday cup were too low and the energy spread too wide. This was due to a large dead spot in the potential gradient within the grid, which permitted a space charge to build up and inhibit ion flow. The solution was to weld a fine nickel mesh around the outside and bottom of the grid and to provide a small grounded tube above, to extract and accelerate the ions. The actual geometry was modeled by solving the Laplace equation for the potentials within the grid and tube, which predicted that we should obtain monomer ion energies of 65 to 75 eV. This was confirmed experimentally as shown in Figure 30 for ionized silver.

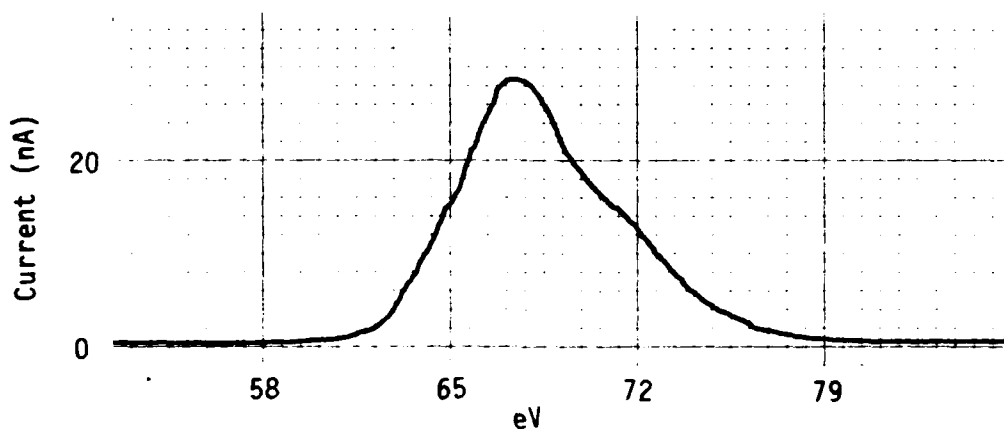


Figure 30. Energy spread of extracted ions.

Detection of the beam flux and current was done with a crystal rate monitor, an electrostatic energy analyzer, and a shielded Faraday cup (see Figure 25). A slot was cut in the analyzer and the contour replaced with a fine mesh so that the rate monitor could measure neutral beam flux on-axis, while the analyzer and cup measured ion current on-axis. The basic principle of a cylindrical electrostatic analyzer can be easily understood from Figure 31. In essence, it is a device which creates a nearly uniform radial field; by setting the electrode voltages one can select particles of a given energy while others collide with the walls. The analyzer was constructed in accordance with the design rules by Septier (1967) to give near-theoretical performance and focusing along the slit dimension. The analyzer had a range of 0 to 800 eV and a resolution of about 4%.

The Faraday cup was made in the shape of an elongated box to match the dimensions of the analyzer exit slit. This maximized the detection efficiency without adding much to its capacitance. Shielding was provided (not shown in Figure 26) to keep out stray electron currents. Shielded cables routed the current signals to an external amplifier.

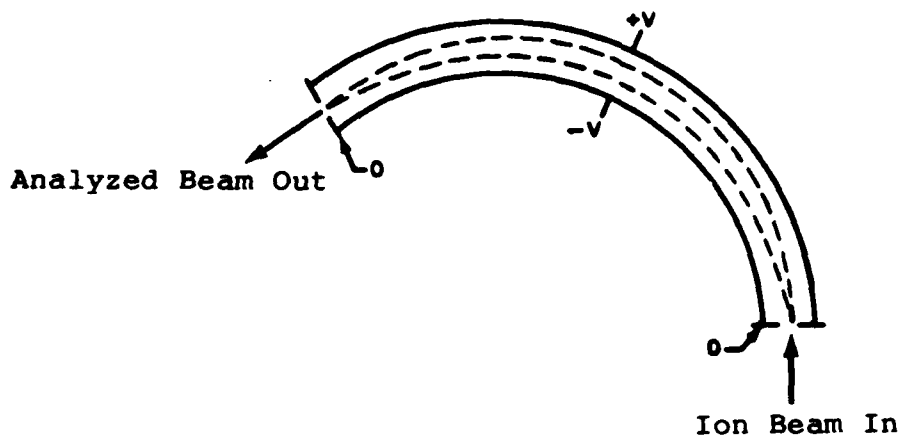


Figure 31. Focusing electrostatic analyzer.

### 5.3. Beam Ionization and Detection

#### 5.3.1 Cross Section for Electron Impact Ionization

An important goal of this work was to obtain quantitative information regarding the makeup of a cluster beam. Electrostatic methods can be applied to separate charged species by mass, but it is much more difficult to analyze the neutral species. One method which has sometimes been tried is to look at TEM grids which have been given a low-coverage deposit and assume that the islands which are seen correspond to actual clusters. This method has worked well for gas-evaporated particles which impact at low velocity, and where a continuum of sizes from microns down to a few nanometers can be produced and studied. We were hesitant to use it in the present investigation, however, because we expected that most of the beam flux would be in the form of single atoms rather than clusters. Because atoms deposited on a surface will nucleate into small islands of their own it would be difficult to draw any firm conclusions from such studies.

Instead, one can try to find the neutral population by counting the cluster ions and then working backwards. This requires that some estimate be obtained for the ionization cross section of the clusters, and also that the ionizing apparatus be well characterized. This is the approach which we followed.

Few if any data are available for the ionization cross sections of clusters. A recent and comprehensive book on impact ionization by Mark (1985) contained only two or three pages on clusters, and made no mention of data for metal clusters. In the absence of direct data, estimates must be made by geometric considerations and extrapolations from atomic ionization cross sections. The cross section for ionization of silver atoms is shown in Figure 32. As is typical for virtually all atoms and molecules, the curve peaks at an energy several times the ionization potential and then gradually decreases at higher energies. Takagi (1975) published a curve for ion current vs. electron energy with a lead cluster beam which showed the same general behavior; other than his curve no data have been found which pertain to metal clusters.

One cross section estimate can be had from the geometrical cross section alone. Thus

$$\sigma(N) = A = \pi(3Nv/4\pi)^{2/3}$$

where A is the frontal area, N the number of atoms in a cluster, and v the volume per atom. Using silver clusters of 1000 atoms as an example leads to a cross section of  $8.1 \times 10^{-14} \text{ cm}^2$ . This method was used by Kuiper et al. (1981) in their study of cluster sources. It is obviously a crude approximation, since the cross section can have no energy dependence.

Another estimate (and probably an upper bound) comes from treating the atoms in a cluster as completely independent particles. Then  $\sigma(N) = N\sigma(1)$ . Again using 1000 atom silver clusters, this leads to  $\sigma = 4.6 \times 10^{-13} \text{ cm}^2$  at 75 eV.

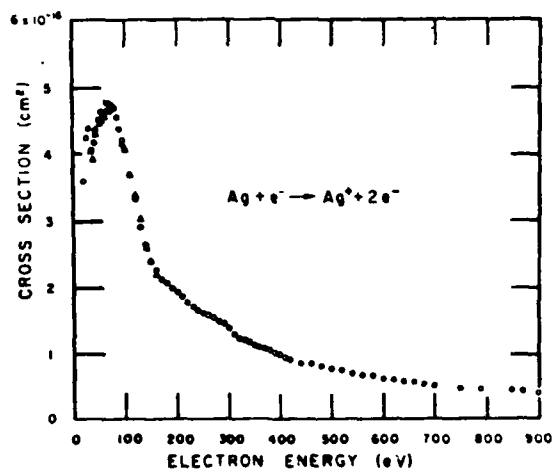


Figure 32. Electron impact ionization cross section for silver (from Crawford, 1967).

A third way which seems preferable is to treat the atoms as independent, but to include a penetration depth factor. Mean free path data for electrons in solids can be used such as those given in Somarjai (1981). For 75 eV electrons in silver this depth is 0.5 nm, considerably less than the expected cluster diameters of about 3 nm. Multiplying the depth by the surface area of the cluster and the atom density gives the number of atoms sampled by the electron, about 230 for a 1000 atom cluster. Then  $\sigma = 230 \times \alpha(1) = 1.1 \times 10^{-13} \text{ cm}^2$ . Interestingly enough, this value is quite close to that given by the frontal area. However, this holds true only near the energy at which the atomic ionization peaks. At higher or lower energies this method will reflect the general tendencies of the atomic ionization curve, as modified by the penetration depth factor. At 350 eV this gives  $\alpha(1000) = 5.6 \times 10^{-14} \text{ cm}^2$  for the cluster.

A valid objection which might be raised is that the metal clusters really ought to behave more like a bulk metal. We considered several ways of accounting for this, principally by applying classical and empirical models for atomic ionization. The atomic models were modified by replacing the atomic ionization potential with the metal work function and then summing over the quasi-independent atoms. As a test, we tried to reproduce the energy dependence which was shown in by Takagi for lead clusters. With all the models tried, the peak occurred at much too low an energy. Whether this is due to the weaknesses of the model or the available data is uncertain.

We expect that better experimental data and models will someday be available for cluster cross sections. At present, there does not seem to be any better way of estimating these quantities than by the method of summing over independent atoms within the penetration depth of the electrons.

### 5.3.2 Detection Efficiency of Apparatus

Careful measurements of the performance of the ionizer and electrostatic analyzer were needed so that we could make quantitative statements about the beam composition. These measurements included: 1) total rate of gas ion production vs. chamber pressure; 2) total rate of metal ion production vs. flux or deposition rate; and 3) the fraction of ions which were extracted from the ionizer, passed the entrance slit of the analyzer, and were transmitted to the Faraday cup.

The rate of gas ion production was important both as a check on operation and so that such currents could be subtracted from the metal ion current later on. This was done by temporarily placing a biased collector wire in the center, just as in a normal ion gauge. After pumping the chamber down to less than  $10^{-7}$  torr and outgassing the ionizer, the chamber valve was closed and the ion collector current read as the pressure slowly increased. Linear relationships were established between collector current and pressure, and between collector current and grid current, with the result that  $I = 23 \text{ mA/torr-mA}$ . The residual gas was primarily water vapor, which is nearly equivalent to nitrogen in ionization probability. For comparison, the published ionization gauge sensitivity is  $10 \text{ mA/torr-mA}$  for nitrogen. This is reasonable agreement considering that element spacings can be quite critical in gauge tubes.

Total metal ion production was measured in a similar way, except that beam flux replaced residual pressure as a parameter. The result was that  $I = 13.2$  nA/mA-Å/s for silver, where the flux was measured by a crystal rate monitor 17 cm above the source. In a typical beam experiment with a 5 Å/s rate and 10 mA of grid current the metal ions would account for 660 nA. This is well above the roughly 20 nA contribution from ionized residual gas at  $10^{-7}$  torr.

With the collector wire removed, the ionizer extraction and analyzer transmission efficiencies were measured. For the metal ions and a 0.5 by 2 cm slit, 42% of the beam or 5.6 nA/mA-Å/s was collected. This is much higher than the 1% or less typical of most mass spectrometer ionizers, in which the extraction field gradient must be reduced to maintain high resolution.

The evidence which was sought for cluster formation was an ion current signal at a substantially higher energy than the 75 eV or so given to all charged species in the ion extraction process. A cluster with  $N = 1000$  will have a kinetic energy of about  $1000 \times 5/2 kT = 350$  eV before being ionized, and 425 eV after ionization and extraction. In order to find the mass fraction  $F(N)$  of the beam which is in the form of  $N$ -atom clusters, the beam current  $I(N)$  at high energy can be compared with the low energy monomer current  $I(1)$  provided that the ionization cross sections are taken into account:

$$\frac{F(N)}{F(1)} = \frac{\sigma(1)}{\sigma(N)} \frac{I(N)}{I(1)} \times N$$

where  $\sigma(N)$  is the cluster cross section,  $\sigma(1)$  the monomer cross section, and the factor of  $N$  accounts for the mass per ion. It is assumed that the monomer fraction  $F(1)$  accounts for most of the beam mass ( $F(1) \approx 1$ ).

The detection limit for cluster population depends on the cluster size and also on the signal to noise ratio at the Faraday cup amplifier. With the analyzer tuned away from the monomer ion peak the noise limit was 0.006 nA peak-to-peak, five orders of magnitude below the typical metal ion current. The finite resolution of the energy analyzer must also be taken into account by calculating the equivalent mass range sampled within the FWHM. For  $N = 1000$ ,  $dM = 40$ . Thus the beam fraction within this range will be given by

$$F(980-1020) \approx \frac{\sigma(1)}{\sigma(1000)} \times \frac{I(980-1020)}{I(1)} \times 1000$$

Inserting  $\sigma(1000) = 1.1 \times 10^{-13}$ ,  $\sigma(1) = 4.6 \times 10^{-16}$ ,  $I(980-1020) = 6$  pA (the noise limit) and  $I(1) = 450$  nA (typical) gives  $F(980-1020) = 5.6 \times 10^{-5}$ . A similar calculation for  $N = 500$ ,  $\sigma(500) = 6.9 \times 10^{-14}$ , gives  $F(488-512) = 4.4 \times 10^{-5}$ . To a good approximation, these results can be extrapolated to find the detectable mass fractions over broader size ranges:

$$F_{\text{det}}(400-600) \approx 3.7 \times 10^{-4}$$

$$F_{\text{det}}(800-1200) \approx 5.6 \times 10^{-4}$$

The 800 to 1200 atom range was chosen because it represents a fair sample of the cluster distribution reported by Yamada (1981). The 400 to 600 range corresponds to the results of Knauer (1987). These two examples and the text above show what we believe our detection limits were during the nozzle beam experiments and how we arrived at them.

#### 5.4 Performance of Nozzled Crucibles

##### 5.4.1 Results of Cluster Detection Experiments

Data published by Takagi show that clusters are most numerous at a vapor pressure of a few torr, and virtually disappear outside the range 1 to 5 torr. Vapor pressure tables for liquid metals show considerable scatter, but a 3 torr pressure ought to occur in the range 1820 to 1900 K for aluminum and 1575 to 1675 K for silver. The vapor pressure changes by about a factor of three with a 100 K change for either material. In most of our experiments two tungsten/rhenium thermocouples were used, one in the body of the crucible and the other in the nozzled lid.

A more direct means of determining the vapor pressure is through measuring the rate  $\dot{m}$  of mass flow from the crucible and using the following relation for a sonic nozzle:

$$\dot{m} = \sqrt{\frac{\alpha \gamma (\gamma + 1)}{2RT_S}} P_S (2/(\gamma + 1))^{\gamma/(\gamma - 1)} A_0$$

where  $A_0$  is the nozzle cross sectional area,  $\alpha$  the molar mass,  $R$  the gas constant, and  $P_0$  and  $T_0$  the pressure and temperature in the crucible.  $\gamma$  is taken to be 5/3, the specific heat ratio for a monatomic gas.

Experimentally, the mass flow rate was determined to an accuracy of 10% or better by weighing the metal charge in the crucible, evaporating part of it at a nearly constant rate, and then re-weighing afterwards. As an example, a flow rate for silver of  $1.6 \times 10^{-3}$  gm/s was obtained with a 1.25 mm orifice, which by the above relation gives  $P_0 = 4.8$  torr. A thermocouple on the crucible body read  $T_0 = 1706 \pm 20$  K, well within the range expected from vapor pressure tables.

In our first series of experiments, aluminum was used because of its usefulness as an optical and electronic material. It was evaporated from boron nitride crucibles to avoid reactions, which other cluster beam workers had noted when using aluminum in graphite. Electrostatic analyzer data were taken from 0 to 800 eV for  $P_0(\text{Al}) = 0.5, 1.6, \text{ and } 3.5$  torr. A 10 mA grid current at 75 eV was used for ionization, giving a monomer peak of over a hundred nA at 3.5 torr. No other peaks were seen. The lid in this case was about 50°C cooler than the body of the crucible, which should not be important if clustering occurs in the gas flow rather than on surfaces.

In the absence of a detectable peak, an upper limit for cluster population can be established. This limit is determined by: 1) the signal to noise ratio of the detection electronics; and 2) the ionization cross section of a cluster. Both of these were discussed in the preceding sections and a detection limit arrived at for silver. In the early aluminum experiments the noise level was somewhat higher, about 0.1 nA, but a similar analysis leads to the following upper limits for cluster mass fractions in the 500 and 1000 atom ranges:

$$F_{Al}(400-600) \leq 6.1 \times 10^{-3}$$
$$F_{Al}(800-1200) \leq 9.3 \times 10^{-3}$$

After these initial results we received a preprint outlining the heterogeneous growth mechanism (Knauer, 1987). This model was discussed in Section 4.5. Among its predictions is that aluminum should not form clusters in a cluster beam source because aluminum will wet virtually any crucible material at high temperatures. This implies that clusters growing heterogeneously on crucible surfaces will adhere too strongly to be ejected by phonon excitation. This led us to try silver instead of aluminum in subsequent experiments.

In the silver experiments, special care was taken to keep the crucible lid and orifice only slightly cooler than the crucible body temperature. This was done to keep conditions within the range predicted by Knauer for heterogeneous nucleation. This degree of temperature control is not easy to achieve at high temperatures because of the large radiation losses and the difficulty of maintaining good thermal conduction paths, plus the difficulty of making good temperature determinations. If the heterogeneous mechanism is correct, the best approach to crucible design would include a separate heater and power supply for the lid and orifice region. This was not possible in the Phase I study. However, by using two heat shields over the crucible lid and a long threaded connection between the parts the lid temperature could be kept to  $-20 \pm 10^\circ\text{C}$  of the body. A finite difference model of the radiant and conductive heat transfer was used to predict the lid temperature; this served as an aid to design and a check on the reasonableness of the thermocouples. An example of the crucible designs is shown in Figure 33.

Crucibles of both boron nitride and a carbon-loaded graphite were used in the silver beam experiments. Also, some of the nozzles had a simple 1 x 1 mm cylindrical profile while others had a tapered section as was shown in Figure 33. In the course of checking various ideas many trials were made, which eventually covered most of the pressure range between 0.3 and 16 torr. Figures 34 and 35 are relatively unadorned original data typical of the runs made, showing control over temperature and deposition rate, and an energy-analyzed beam current spectrum.

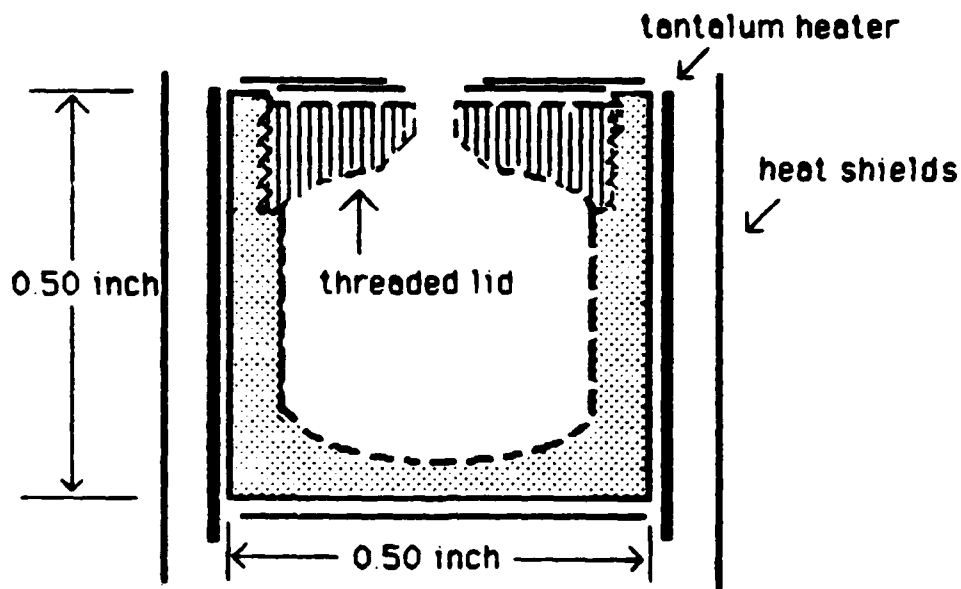


Figure 33. Crucible design for minimizing temperature differential.

Considerable evidence was accumulated which pointed toward the heterogeneous mechanism for cluster growth, including the ejection of fine droplets under certain conditions. These results will be discussed in the next section. However, the electrostatic analyzer data did not show the presence of clusters in the nanometer size range of about 20 to 2000 atoms each.

An upper bound for the silver cluster population is then given by the detection limit, which was derived in the previous section. Thus

$$F_{Ag}(400-600) \leq 3.7 \times 10^{-4}$$

$$F_{Ag}(800-1200) \leq 5.6 \times 10^{-4}$$

when  $P_0 = 9$  torr. At  $P_0 = 3$  torr the upper limit is about a factor of two higher because of the lower monomer current.



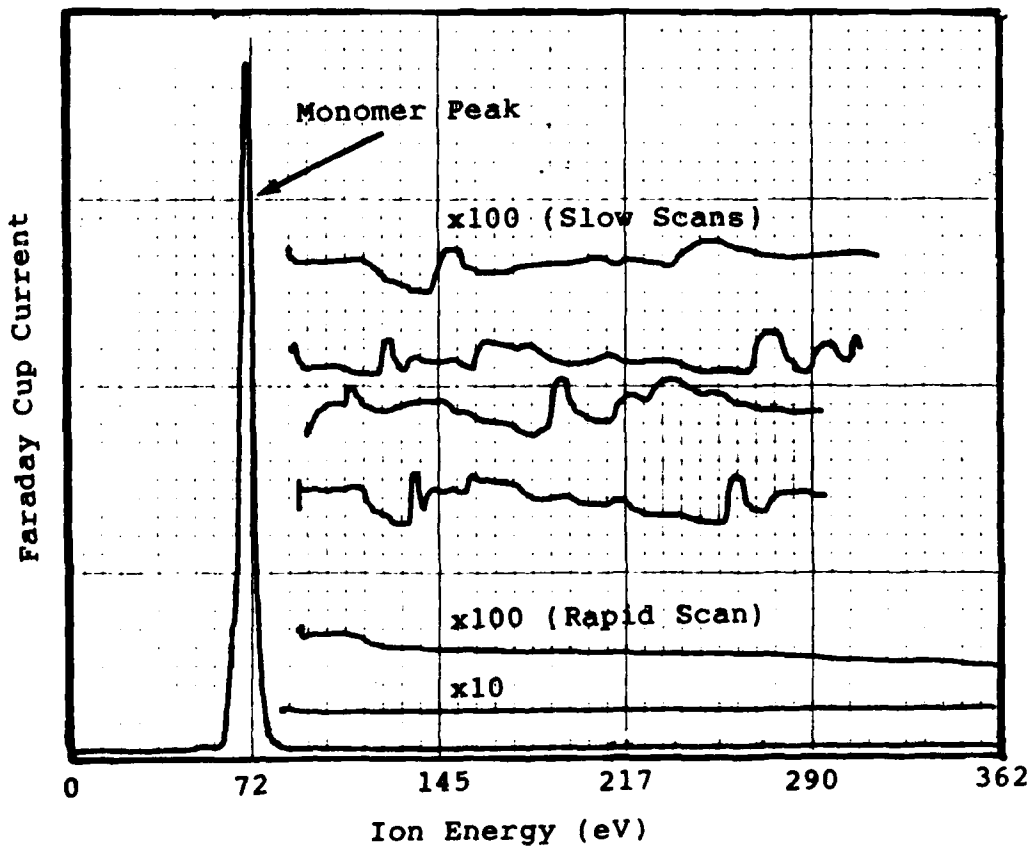


Figure 35. Example of electrostatic energy analyzer results.

The flow field from the nozzle had been modeled previously, as described in Section 3.2. From this information it is possible to predict the thickness distribution of a film deposited on a substrate. As a test of the reasonableness of the gas flow modeling, several semitransparent silver films were deposited for comparison. Film thickness profiles were determined from densitometry and calculations using the optical constants of silver. The results for nozzle beam deposition with  $P_0 = 1$  torr are shown in Table II. The agreement is found to be quite good, with the predicted profile being peaked in comparison with an effusive source and the measured profile peaked slightly more. The calculations were carried out up to an angle where more than half the beam mass was accounted for ( $M_\theta > 0.5$ ), although the substrate subtended only  $20^\circ$ .

Table II. Predicted Versus Measured Thickness Profile

R/R <sub>N</sub>	$\theta_{\text{final}}$ (deg)	$M_\theta$	Actual (nm)	Predicted (nm)	Effusive Source (nm)
0.0	0.00	0.00	50.0	50.0	50.0
0.1	4.04	0.01	49.1	49.3	49.5
0.2	7.98	0.04	46.7	47.6	48.1
0.3	11.96	0.09	42.1	44.4	45.8
0.4	16.11	0.16	38.9	40.2	42.6
0.5	20.61	0.25		34.7	38.4
0.6	25.34	0.36		28.3	33.4
0.75	33.40	0.54		17.6	24.3

R/R<sub>N</sub> = Starting position of streamtube in nozzle, expressed as radial distance from centerline. (R/R<sub>N</sub> = 0.0 on centerline, = 1.0 at nozzle wall).

$\theta_{\text{final}}$  = Final angle of streamtube from R, calculated by method of characteristics.

$M_\theta$  = Fraction of total beam mass within  $\theta_{\text{final}}$ .

#### 5.4.2 Evidence for Heterogeneous Growth of Fine Particles

The experiments described in the previous section seem to show that significant metal cluster growth cannot occur through homogeneous nucleation mechanisms. In spite of this result, other mechanisms cannot be ruled out. One which seems plausible is heterogeneous nucleation at inner surfaces of the crucible. Knauer (1987) has worked out a reasonable theory for this mechanism which can, given certain assumptions, predict that clusters form (see Section 4.5). The requirements include a slightly cooler surface which experiences a high flux of metal vapor and non-wetting (weak bonding) of cluster material to the crucible. If the temperature difference is small, clusters should detach from the walls before growing appreciably and may then be entrained in the vapor flow.

The theory gives temperature ranges in which clusters could be formed by this mechanism. Several of the cluster detection experiments were run in or near this range, with  $\Delta T = -20 \pm 10^\circ\text{C}$ . While no clusters of  $N$  less than 2000 atoms were observed, it should be added that the predicted range is probably somewhat sensitive to the data and assumptions fed into the model, and only the general trends of the theory have been verified by Knauer so far. Also, the ultimate cluster/particle size should be a sensitive function of the crucible temperature differential, as was shown in Figure 23. Besides electrostatic analyzer measurements, some TEM grids were briefly exposed to the beam and analyzed by Ken Westmacott at the National Electron Microscopy Center at Lawrence Berkeley Laboratory. These did not show evidence of clusters.

Positive evidence for the surface (heterogeneous) growth mechanism was obtained by observations of larger particles. In some runs droplets were ejected from the orifice, ranging in size from 100 nm to several microns. A silver coating which includes many such particles is shown in Figure 36. Some of the smallest particles seen are shown in Figure 37, in which a film of 3 nm average thickness was deposited on carbon. The many small patches in the background are islands of silver which nucleated on the substrate from the monomer component of the beam. It is clear that the particles are not merely the upper end of the island size distribution.

The ejected particles could be directly correlated with the metal deposits formed on the underside of the crucible lid near the orifice. The low thermal mass of our crucibles allowed us to cool them at nearly  $15^\circ\text{C/s}$ , rapidly lowering the metal evaporation rate and preserving most of the deposits. Surface properties appeared to correlate with particle presence in two ways: 1) material combination, and 2) surface finish of the orifice region.

The material combinations investigated were: aluminum in BN crucibles; silver in BN; and silver in carbon-filled graphite. The aluminum both wet and reacted with BN, as shown in Figure 38, and no particles were ejected from the orifice. Likewise, no particles were seen with silver in BN, even though this is considered to be a non-wetting combination. Figure 39 of the orifice region shows that particles do form there but that the area of surface contact is still quite large. However, a much higher contact angle of about  $135^\circ$  was observed for silver on carbon (Figure 40) and particles were ejected under certain conditions. This correlation of particle ejection with low surface bonding strongly suggests that Knauer's theory of heterogeneous cluster growth is basically correct.



Figure 36. Silver coating formed from nozzle beam source.

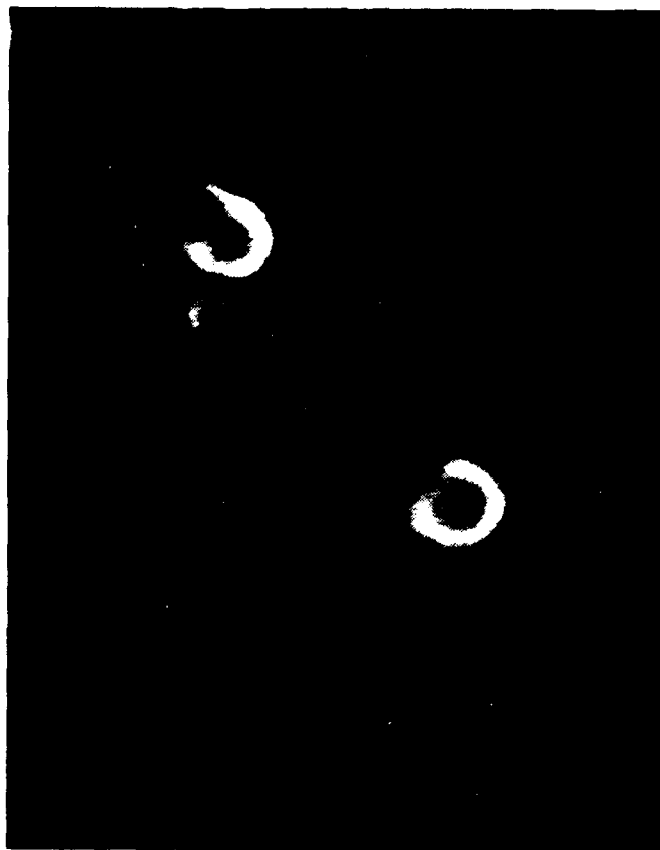


Figure 37. Silver particles and island structure from nozzle beam source.



Figure 38. Aluminum reacted with boron nitride crucible lid.



Figure 39. Silver droplets on boron nitride crucible after heating.



Figure 40. Silver droplets on carbon crucible after heating.

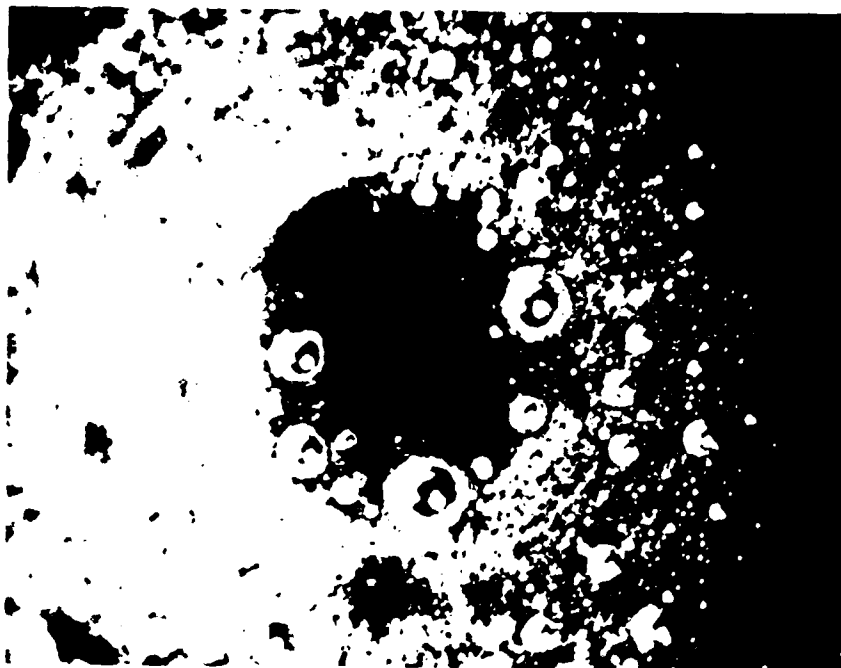


Figure 41. Effect of surface finish on droplet formation in crucible.

Another interesting observation was that particles were much more likely to be ejected when the orifice region had a relatively coarse finish. Figure 41 shows the underside of a crucible lid in which the center portion has been smoothed. A few large particles appear in the smoothed portion but it is otherwise clear. This is hard to explain, since roughness ought to bring about more complete wetting and stronger bonding. A reasonable explanation is that roughness holds the droplets more tenaciously, during the growth period, so that they reach a size which is observable with our SEM. The very large particles are probably the result of coalescence. In any case, the correlation of particle ejection with surface properties supports the heterogeneous growth hypothesis.

#### 5.4.3 Growth of Ultrafine Particles or Clusters by Gas Quenching

The apparent difficulty of making metal clusters with a Takagi-type source led us to explore other methods. This was a natural extension of the original scope of work and has already opened up new options for future research.

Gas quenching is one technique for obtaining particles reliably and with considerable control over the final particle size. In its simplest form, a metal can be heated in an open boat to a vapor pressure of a few torr and the vapor quenched in a quasi-static inert gas. The nucleation and growth of particles is then controlled by the pressures and by the velocity at which the gas passes over the metal source. Typically, convection currents in the meter per second range are allowed to control the gas velocity and the particles drift toward collection surfaces. A source of this type is shown in Figure 42. Granqvist (1976) performed a thorough study of the pressure dependences and found that more or less monodisperse particles could be formed with any desired size from a few nanometers to hundreds of nanometers.

This simple form is similar in principal to the pulsed laser vaporization sources now used widely in cluster science. The pulsed sources provide tiny quantities of small clusters ( $N < 40$ ); the clusters and carrier gas can then be formed into supersonic beams for spectroscopic studies. Velocities of hundreds of meters per second are obtained.

An ultrafine particle source suitable for coating deposition might be developed by using parts of both methods. A boat or oven can efficiently vaporize large quantities of material into a quenching gas, and the resulting particles entrained in a nozzle flow to provide initial acceleration. Figure 43 illustrates this concept. A number of issues arise in properly designing such a source, such as: maintaining the desired gas velocity over the metal source (to minimize or control convective forces); keeping the particles in the center of a laminar flow to avoid orifice fouling; creating flow convergence patterns into the nozzle which do not lead to centrifugal settling of particles out of the flow; differential pumping of the downstream portion to remove or recycle the carrier gas and allow deposition under moderate vacuum. The proposal for Phase II of this program addresses these in some detail. Ultimately, a combination of gas flow modeling and experimental development will be needed.

To conclude the Phase I development effort, a proof test was conducted of gas-quenched particle growth. Silver was evaporated from our nozzle beam source at a high rate into 1 torr of argon. An open crucible could have been used to the same end (see Figure 42), but the nozzled source gave the metal vapor a more uniform flow velocity in the nucleation zone and should therefore result in a narrower distribution of particle sizes. Of course, beyond the first few millimeters the particle/gas mixture should have slowed to a speed determined by convection in the static chamber.

An SEM photo of the resulting particles is shown in Figure 44. The deposit consisted of fine particles of approximately 50 to 100 nm, loosely agglomerated as expected. Formation of a dense coating will require entrainment of the particles in a converging nozzle flow along the lines of Figure 43. However, the basic idea of gas-quenched growth seems to be sound, and the nozzled crucible for the metal vapor may be useful in developing the overall source.

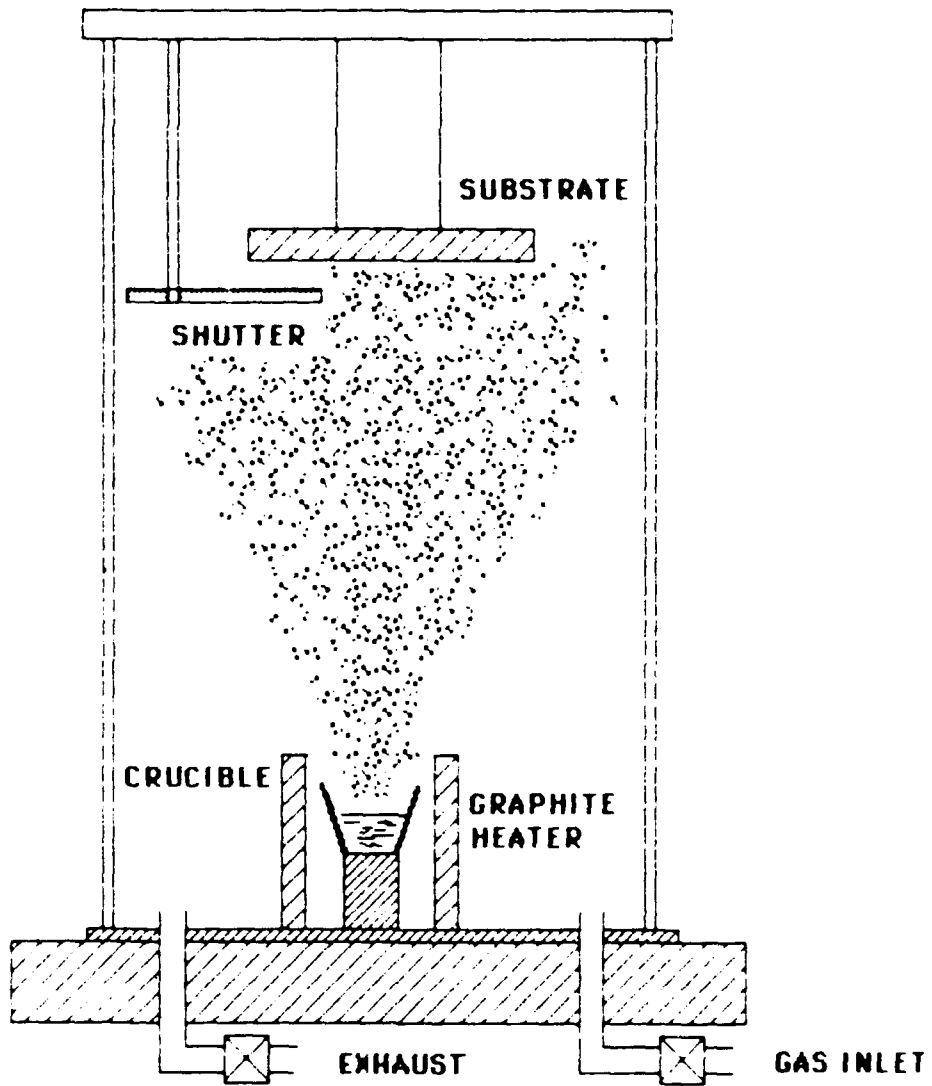


Figure 42. Particle growth in closed chamber free with convective transport.

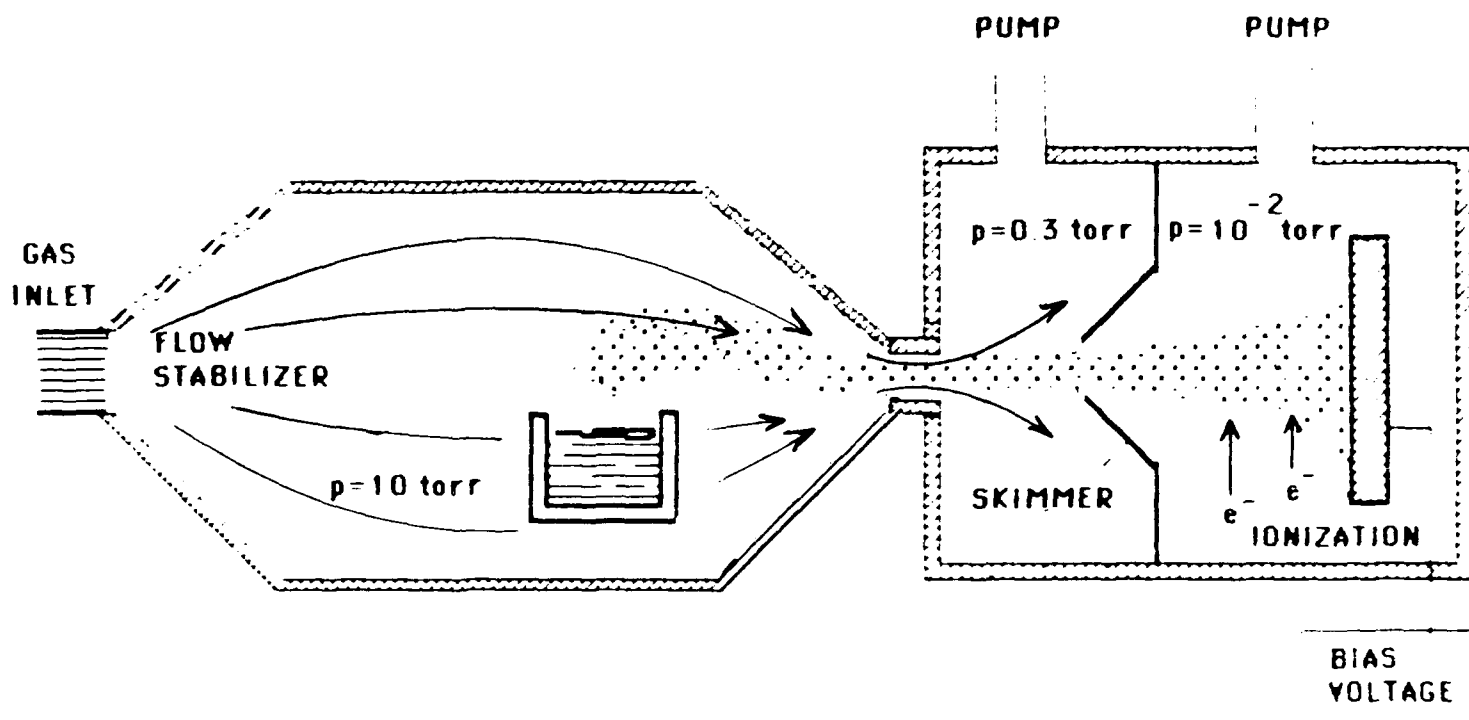


Figure 43. Flow-controlled ultrafine particle generation and deposition.

For optical material applications a smaller particle may be more desirable. The literature indicates we could reach this range with a metal source which gives a lower supersaturation, such as an ICB-type crucible with a larger orifice at lower temperature. A lower argon pressure or helium instead of argon should also reduce the particle size (Granqvist, 1976).

Gas-quenched techniques are especially interesting because of the range of particle sizes obtainable. Thus, it may be possible to enormously broaden the range and possibilities of "cluster" deposition. At the 2 - 3 nm end of the scale are large clusters of roughly a thousand atoms, similar to those considered by Takagi for epitaxial deposition. With a high fraction of surface atoms, it is intuitively plausible that such clusters should break up into individual atoms on impacting a substrate at high velocity (see Figure 2). Larger clusters of 5 - 10 nm or more might more properly be termed ultrafine particles. With fewer surface atoms, these should retain more of their particulate character and may form coatings by flattening or "splattling" on a substrate (see Figure 3). This would be more in line with the structure of plasma sprayed coatings, but on a much finer scale. Because plasma sprayed coatings do not show the columnar structure of most thin films, deposition of ultrafine particles may provide significant advantages for optical films.

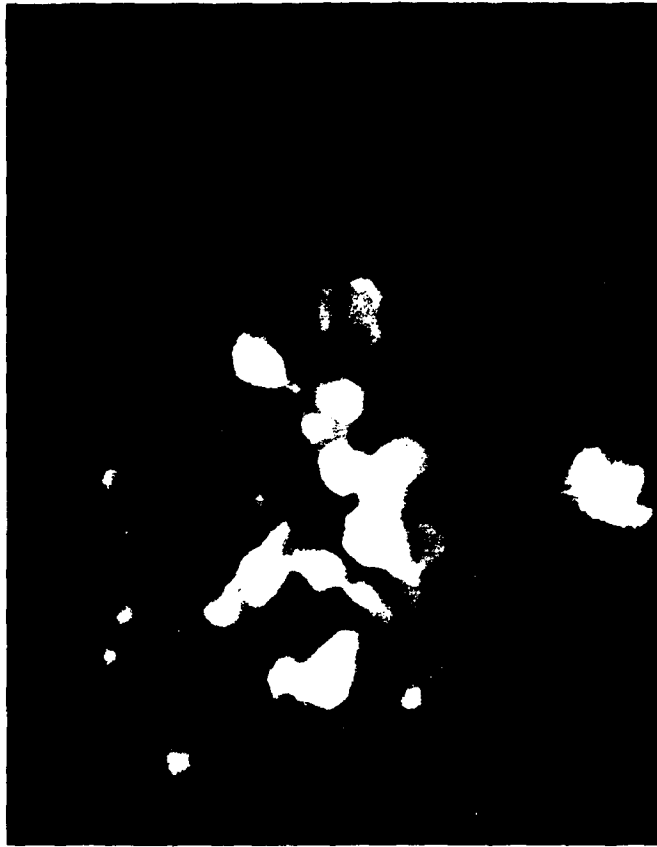


Figure 44. SEM photo of 50-100 nm silver particles produced with nozzled crucible and argon quenching.

## REFERENCES

- Crawford, C., and Wang, K., J. Chem. Phys. 47 (11), 4667 (1967).
- Dahlquist, G., and Björk, A., Numerical Methods, Prentice-Hall, Englewood Cliffs, N.J., 1974.
- Frenkel, Kinetic Theory of Liquids, Oxford University Press, Oxford (1940).
- Granqvist, C. G., and Buhrman, R. A., "Ultrafine Metal Particles," J. Appl. Phys. (47) 5, p. 2200 (1976).
- Hagena, O. F., in Molecular Beams and Low Density Gasdynamics, P. P. Wegener (ed.) Dekker (1974).
- Hill, P. G., J. Fluid Mech., 25(3), 593 (1966).
- Kantrowitz, A., and Grey, J., Rev. Sci. Inst. 22, 328 (1951).
- Knauer, W., J. Appl. Phys. 61 (6) (1987).
- Knauer, W., "Formation of Large Metal Clusters by Surface Nucleation," International Workshop on Ionized Cluster Beam Technique, Tokyo (June 1986).
- Kreibig, U., and Fragstein, C. V., Z. Phys. 224, 307 (1969).
- Kuiper, A. E. T., Thomas, G. E., and Schouten, W. V., J. Cryst. Gr. 51, 17 (1981).
- Märk, T. D., in Electron Impact Ionization, T. D. Märk and G. H. Dunn (ed.), Springer-Verlag, Vienna, 1985.
- Müller, K.-H., J. Appl. Phys. 61 (7), 2516 (1987).
- Septier, A., Focusing of Charged Particles, Academic Press, New York (1967).
- Shapiro, A. H., The Dynamics and Thermodynamics of Compressible Fluid Flow, Volume II, Ronald Press, New York, Chapter 17 (1954).
- Somorai, G., Chemistry in Two Dimensions: Surfaces, Cornell University Press, Ithaca, New York (1981).
- Takagi, T., Yamada, I., Sasaki, A., J. Vac. Sci. Technol., Vol. 12, No. 6, 1128, (1975).
- Takagi, T., in Emergent Process Methods for High Technology Ceramics, ed. R. F. Davis, Plenum Press, New York (1984).
- Takagi, T., J. Vac. Sci. Technol., A 2(2), 382 (1984).

REFERENCES (Cont.)

Usui, H., Ueda, A., Yamada, I., Takagi, T., Proc. 9th Symp. on ISIAT, Tokyo, 39 (1985).

Windischmann, H., Pruett, J., Nicholas, M., and Lampard, P., paper G3-2 presented at 1987 Spring Meeting of the Materials Research Society, Anaheim, California.

Yamada, I., Takagi, T., *Thin Solid Films*, 80, 105 (1981).

Yang, S.-N., and Lu, T.-M., *Appl. Phys. Lett.* 48 (17), 1122 (1986).

## APPENDIX - SUPPLEMENTARY INFORMATION

### Personnel

#### Principal Investigator

Arther C. Day, M.S. Applied Physics, University of Washington, 1983.  
Thesis: "Analysis of Surfaces by Rutherford Backscattering."

#### Contributors

Julian A. Domaradzki, Ph.D., Physics, Institute of Theoretical Physics, Warsaw, Poland.

G. S. Knoke, Ph.D., Aeronautics and Astronautics, University of Washington, 1975. Thesis: "Combusted Ludwig Tubes for Gasdynamic Laser Research."

R. P. Turcotte, Ph.D., Physical Chemistry, Arizona State University, 1969. Thesis: "I. High-Temperature X-Ray Studies of Widely Nonstoichiometric Regions in the Praseodymium Oxide-Oxygen System; II. Structure and Thermal Stability of the Rare Earth Carbonates and Formates."

### Inventions

Section 4.4.3 of this report discussed two concepts that may be considered inventions. Their development was outside the original scope of work and did not result in additional contract change; however, they are a logical extension of the Phase I effort and are relevant to future work as contemplated in the Phase II proposal. They are:

1. Gas-quench assisted formation of ultrafine particles with nozzle beam source.
2. Laminar flow enclosure for transport of ultrafine particles and separation from quench gas.

### Publications

The following papers cover work performed on or related to the Phase I contract and are planned for submission in August 1987:

"Emissivities and Cooling Rates for Hot Clusters," A. C. Day, to be submitted to Applied Physics Letters or Journal of Applied Physics.

"Mechanisms for Cluster Formation and Deposition: Limitations and Possibilities," A. C. Day, J. A. Domaradzki, G. S. Knoke, to be submitted to Journal of Vacuum Science and Technology.